Numerical methods and macroscopic models of magnetically confined plasmas for propulsion

Fabrice Deluzet, Jacek Narski, Moctar Ndiaye, Gerjan Hagelaar, Jean-Pierre Boeuf

Numerical methods and macroscopic models of magnetically confined plasmas for propulsion

F. Deluzet[‡,*], J. Narski[‡], M. Ndiaye[‡], G. Hagelaar[†], J. Boeuf[†]

[‡]Université de Toulouse; UPS, INSA, UT1, UTM,
Institut de Mathématiques de Toulouse,
CNRS, Institut de Mathématiques de Toulouse UMR 5219,
F-31062 Toulouse, France,
forname.name@math.univ-toulouse.fr

[†]LAPLACE, Université de Toulouse, CNRS, INPT, UPS,
118 Route de Narbonne, 31062 Toulouse, France
forname.name@laplace.univ-tlse.fr

* Corresponding author.

March 25, 2022

Abstract

In this paper a hierarchy of macroscopic plasma models is derived for the numerical study of plasma thrusters. This derivation outlines the multi-scale nature of the problem and the difficulty for numerical methods to address efficiently this challenge. A specific focus is made on quasi-neutral models built on the anisotropic equations of the particles transport. A numerical method is proposed for this class of problems offering an accuracy unrelated to the anisotropy strength without resorting to the approximation of equipotential magnetic field lines.

Keywords Anisotropic equation, Plasma Physics, Asymptotic-Preserving schemes.

1 Introduction

The simulation of plasma propulsion devices [6, 38] represents a significant challenge for the design of efficient numerical methods. This is due to the multi-

*Corresponding author

scale nature of plasma physics [15] in general and specifically in the context of this application. We consider in this paper low temperature magnetized plasmas typical of those of ion sources for space propulsion (e.g. Hall thrusters also called Stationary plasma thrusters, gridded ion thrusters, cusp-field plasma thrusters etc... [6],[38]). The plasma evolution may be described by kinetic models for both the electrons and the ions for the most refined descriptions [14, 9, 29, 5, 7, 26]. Hybrid models [3] rely on a coarser representation of the electrons, this species being described by a fluid model. Finally the ions may also be described by a fluid model [23, 22, 36]. This latter class of models will be specifically investigated in the present work. Though they offer a quite coarse plasma description, they give access to reach enough physics and with an incomparable computational efficiency compared to kinetic descriptions.

The multi-scale nature of the problem exceeds the only questions of the kinetic or macroscopic modellings of the plasma. Generally it also encompasses the quasi-neutrality of the plasma and the small scales attached to the electron inertia. The question related to the quasi-neutrality has received a lot of attention including the treatment of local breakdowns [12, 13, 18, 16, 11, 1, 2]. Quasi-neutral models filter out the small scales related to charge separations, namely the Debye length and the plasma period. In regions of large plasma densities, these two scales are small compared to that of the device operation. It is therefore interesting to filter out these scales from the equations to derive an efficient simulation tool. In the context, of magnetically confined plasmas, this class of models introduces an specific difficulty. Due to the intense magnetisation of the plasma, the equations are severely anisotropic which represents a major difficulty for numerical methods to produce accurate approximations of the electric field. This issue is identified as the main bottleneck for the derivation of numerical methods based on quasi-neutral models ([30, Sec. III]).

The present work is first dedicated to the derivation of a hierarchy of macroscopic (fluid) models for strongly magnetized plasmas. This study is conducted in order to clarify the different assumptions embedded in the models used in the context of these plasmas and, more specifically, in the context of electric propulsion: plasmas are cold, partially ionized, the ions being non magnetized. This work is restricted to two dimensional geometries containing the magnetic field lines (*i.e.* there is no magnetic field component perpendicular to the two dimensional simulation domain), the aim being the capture of steady states. In particular, the physics developing in the $E \times B$ direction [35] is out of the scope of the present investigations. A derivation of these models, by means of the asymptotic analysis, is therefore proposed together with an emphasis of how these models relate to each other.

In a second part, a more specific attention is paid to the numerical approximation of anisotropic problems providing the electric potential in quasi-neutral models. The difficulty here stems from two different aspects of the problem. The first one is related to the loss of precision of numerical approximations with coordinates and meshes misaligned to the anisotropy (magnetic field) direction [23]. This is analyzed in [41] and explained by an amplification of the discretization error by the large heterogeneity of the parallel and perpendicular

transport coefficients. Furthermore, the condition number of the system matrix stemming from the discretization of the anisotropic problem may increase with the anisotropy strength, depending on the boundary conditions imposed at the magnetic field line ends. Different workarounds are proposed to circumvent this difficulty. The limit problem, obtained by assuming an infinite anisotropy, is proposed to compute the electric field approximation in [23]. This amounts to considering the magnetic field lines as equipotential for the electric potential. Field aligned approaches come naturally into play to address the loss of precision originating from the mesh misalignment. This is the path followed for instance in [33, 32] (in the framework of electric propulsion, see also [39] for ionospheric plasma simulations). Nonetheless, these methods are difficult to extend to complex magnetic field geometries such as cusp-shaped field [25, 37] considered within this document. An original numerical method, free from this constraint, is proposed in [27, 8, 28]. It relies on an hyperbolic formulation of the anisotropic problem satisfied by the electric potential. The solution of the anisotropic problem is approximated by the steady state of a pseudo-time dependant system. The convergence time to this steady state is roughly proportional to the anisotropy strength: the number of pseudo-time iterations is observed to scale as $\varepsilon^{-0.7}$ [27, 8].

In recent studies, the derivation of efficient numerical methods for anisotropic problems has been addressed thanks to asymptotic-preserving schemes [17], initially for field aligned coordinates, this requirements being unnecessary in subsequent developments [16, 19, 20, 40]. These numerical methods are designed to capture the limit regime when $\varepsilon \to 0$. This avoids the blow-up of the condition number of the system matrix and preserve the accuracy of the approximation for increasing anisotropy strength. This class of numerical methods is implemented in the context of magnetically confined plasmas in a range of parameters representative of electric propulsion. A new augmented Micro-Macro method is introduced within this document with the aim to correct the loss of symmetry of the so-called inflow Micro-Macro method [19].

The paper is organized in three sections. The first section is devoted to the derivation of the model hierarchy. It is designed to represent the evolution of an isothermal low temperature plasma confined by an intense magnetic field. The models considered within this hierarchy are fluid models originating from a bi-fluid plasma representation, coupled to Poisson equation providing the electrostatic potential. Different reduced models are then introduced by letting asymptotic parameters vanish, to recover the quasi-neutrality assumption, the massless approximation of the electron and eventually the infinite anisotropy regime. In the second section, the difficulty stemming from the discretization of anisotropic problem is addressed. The set of equations considered for the simulation of magnetically confined plasma is specified including the geometry of the cusp-shaped magnetic field together with a set of boundary conditions representing the inter-electrode chamber into which the plasma is confined. The loss of precision of numerical methods is outlined and a new augmented Micro-Macro method is introduced to address this issue. Numerical investigations are proposed within the third section. A analytic framework is proposed in order to

assess the effectiveness of the augmented Micro-Macro method. The advantage of this test case comes from the fact that an exact solution can be manufactured (analytically) providing a reference exact solution against which the numerical approximation can be compared. This procedure permits the validation of the augmented Micro-Macro method implemented on the complete model for the simulation of the plasma confinement by a cusp-shaped magnetic field. The loss of symmetry of the numerical approximation carried out thanks to the inflow Micro-Macro method is outlined thanks to these numerical experiments, in contrast the approximations provided by the augmented Micro-Macro method respect the expected symmetry properties.

2 A hierarchy of fluid models for plasma propulsion.

2.1 Bi-fluid isothermal plasma modelling coupled to the Poisson equation

The purpose here is to derive a model problem relevant for the simulation of the plasma of ion sources for space propulsion (termed as "plasma thrusters" in the following) in a simplified, but representative, context. This derivation is organized in a hierarchy of models outlining the multi-scale nature of the problem and hereby the difficulty to derive efficient numerical methods for these models. This hierarchy is constructed by letting dimensionless parameters vanish, deriving by this means reduced models.

The starting point is a set of equations for both the ions and the electrons coupled to Maxwell's equations to account for the computation of the electromagnetic field. The properties of the neutral gas are assumed to be known in this simplified problem. Let $(m_\alpha, n_\alpha, u_\alpha, T_\alpha)$ be the mass, density, mean velocity and temperature of the species α, with $\alpha = i, e$ for the ions or the electrons. Assuming that both the electron and ion temperatures are constant and considering mono charged ions, the plasma evolution may be described thanks to the following sets of equations

$$\frac{\partial n_\alpha}{\partial t} + \nabla \cdot (n_\alpha u_\alpha) = S\,, \tag{1a}$$

$$m_\alpha \left(\frac{\partial n_\alpha u_\alpha}{\partial t} + \nabla \cdot (n_\alpha u_\alpha \otimes u_\alpha) \right) + \nabla (n_\alpha k_B T_\alpha) = q_\alpha n_\alpha \left(E + u_\alpha \times B\right) - m_\alpha n_\alpha \nu_\alpha u_\alpha\,, \tag{1b}$$

s q_α being the charge of the particle, $q_e = -e$ and $q_i = e$ with e the elementary charge, k_B the Boltzmann constant, the tensor product of two vectors u and v is denoted $u \otimes v$.

Different collision processes are accounted for: ν_α is the collision frequency of the specie α against the neutrals, the neutral being at rest and, S is the plasma density created or destroyed by ionisation or recombination. Note that the ion-electron collisions are discarded in both the electronic and ionic equations.

The changes in the electromagnetic field are driven by Maxwell's equation however in an electrostatic approximation, the magnetic field induced by the particle motion being assumed negligible compared to the external one. In the end, the charged particles are coupled by the Poisson equation

$$-\Delta\phi = \frac{e}{\varepsilon_0}(n_i - n_e)\,, \tag{2}$$

ε_0 being the vacuum permittivity. The electric field is deduced from the electrostatic potential ϕ thanks to

$$E = -\nabla\phi\,. \tag{3}$$

The set of equations (1–3) define the basis of the hierarchy of (isothermal) models aimed at representing the operation of plasma thrusters.

2.2 The dimensionless bi-fluid-Poisson system

This hierarchy of models is derived thanks to the introduction of asymptotic parameters, introduced in the equations by working with non dimensional quantities. First, some physical quantities are introduced. The cyclotron frequency $\omega_{c,\alpha}$ the mobility μ_α, the Hall parameter $\mathcal{H}_\alpha$ for the species α defined as

$$\omega_{c,\alpha} = \frac{e|B|}{m_\alpha}\,, \quad \mu_\alpha = \frac{e}{m_\alpha \nu_\alpha}\,, \quad \mathcal{H}_\alpha = \mu_\alpha \|B\|\,, \tag{4a}$$

and finally the (electronic) Debye length

$$\lambda_D^2 = \frac{\varepsilon_0 k_B T_e}{e^2 n_e}\,. \tag{4b}$$

Let $\bar{x}$, $\bar{t}$ be the typical length and time scales, these parameters are chosen to capture the flow of the plasma, the electron and ion mean velocity being assumed comparable and denoted $\bar{u}$. This entails to the following scaling relation

$$\bar{u} = \frac{\bar{x}}{\bar{t}}\,. \tag{5a}$$

The plasma is assumed to be close to quasi-neutrality, with comparable electron and ion densities $\bar{n}_i = \bar{n}_e = \bar{n}$. The typical temperature of the species α is denoted $\bar{T}_\alpha$ while $\bar{\nu}_\alpha$ is the typical collision frequency (against neutrals). The simple scaling relation proposed in [24, 4] for the collision frequencies is resumed for this analysis, with

$$\bar{\nu}_e = \sqrt{\frac{T_e}{T_i}\frac{m_i}{m_e}}\bar{\nu}_i\,. \tag{5b}$$

The electromagnetic field scales are denoted $\bar{E}, \bar{B}$ for the electric and magnetic components, with $\bar{\phi} = \bar{x}\bar{E}$. Finally, the typical scale of the ionization term is defined by $\bar{S} = \bar{n}/\bar{t}$.

Non dimensional variables are used to write the equations, with for instance $n_i = \bar{n} n_i'$, the primed quantities being dimensionless. The system (1–2) is recast into

$$\frac{\partial n_i'}{\partial t'} + \nabla' \cdot (n_i' u_i') = S' \,, \tag{6a}$$

$$M_i^2 \left(\frac{\partial n_i' u_i'}{\partial t'} + \nabla' \cdot (n_i' u_i' \otimes u_i') \right) + \theta^{-1} \nabla' (n_i' T_i') = \eta \, (n_i' E') + \bar{\mathcal{H}}_i M_i^2 \kappa_i \, (n_i' u_i' \times B') - \theta^{-1/2} M_i^2 \kappa_i \, (\nu_i' n_i' u_i') \,, \tag{6b}$$

for the ions, together with

$$\frac{\partial n_e'}{\partial t'} + \nabla' \cdot (n_e' u_e') = S' \,, \tag{7a}$$

$$\frac{1}{\kappa_e} \left(\frac{\partial n_e' u_e'}{\partial t'} + \nabla' \cdot (n_e' u_e' \otimes u_e') \right) + \frac{1}{M_e^2 \kappa_e} \nabla (n_e' T_e') = -\frac{\eta}{M_e^2 \kappa_e} \, (n_e' E') - \bar{\mathcal{H}}_e \, (n_e' u_e' \times B') - \nu_e' n_e' u_e' \,, \tag{7b}$$

for the electrons, coupled to the Poisson equation

$$-\eta \lambda^2 \Delta \phi' = n_i' - n_e' \,, \tag{8a}$$

$$E' = -\nabla' \phi' \,. \tag{8b}$$

The system (6-8) is written thanks to the dimensionless parameters defined in Table 1. Note that, the electric energy being measured with respect to the electron internal energy by means fo the parameter η definition, scales attached to the electrons (temperature) are introduced into the dimensionless ionic equations (parameters θ and η).

Table 1: Definition of the dimensionless parameters.

$\mathfrak{m}^2 = \dfrac{m_e}{m_i}$	electron to ion mass ratio;
$\lambda = \dfrac{\lambda_D}{\bar{x}}$	scaled Debye length;
$\theta^2 = \dfrac{\bar{T}_e}{\bar{T}_i}$	electron to ion temperature ratio;
$\kappa_\alpha = \bar{\nu}_\alpha \bar{t}$	number of collisions against neutral during a typical time;
$\bar{\mathcal{H}}_\alpha = \bar{\mu}_\alpha \bar{B} = \dfrac{\bar{\omega}_{c,\alpha}}{\bar{\nu}_\alpha}$	Hall parameter;
$\Omega_{c,\alpha} = \omega_{c,\alpha} \bar{t}$	number of cyclotron rotations during a typical time;
$M_\alpha^2 = \dfrac{m_\alpha \bar{u}^2}{k_B \bar{T}_\alpha}$	squared Mach number for species α;
$\eta = \dfrac{e \bar{x} \bar{E}}{k_B \bar{T}_e}$	electric energy related to the electronic internal energy.

2.3 Derivation of reduced models

2.3.1 A review of models for magnetized low temperature plasmas

The regimes investigated herein share some properties. First, the electric energy magnitude is assumed to match that of the electronic internal energy, yielding $\eta = 1$. Second, the temperature of the electron is larger than the ionic temperature with $\theta > 1$. This allows to neglect the pressure in the ionic flux equation. The ionic internal and kinetic energies are assumed to have comparable scales, while the collisions of ions against neutral are unimportant in explaining the evolution of this species. Finally, the ions are non magnetized. These assumptions give rise to the following scaling relations

$$\eta = 1, \quad \theta > 1, \quad M_i^2 \sim 1\,, \tag{9a}$$

$$\kappa_i \lesssim 1\,, \quad \bar{\mathcal{H}}_i \lesssim 1\,. \tag{9b}$$

Note that, the relations (9b) yield $\omega_{ci}\bar{t} < 1$ or equivalently, the scale of the velocity being defined by Eq. (5a), $\bar{u}/(\bar{x}\omega_{ci}) > 1$. The typical ionic Larmor radius exceeds the typical length scale, hence the demagnetization of the ions. The equations governing the evolution of this species may be reduced to

$$\frac{\partial n_i}{\partial t} + \nabla \cdot (n_i u_i) = S\,, \tag{10a}$$

$$\frac{\partial n_i u_i}{\partial t} + \nabla \cdot (n_i u_i \otimes u_i) = n_i E\,, \tag{10b}$$

while the electronic macroscopic properties obey the system

$$\frac{\partial n_e}{\partial t} + \nabla \cdot (n_e u_e) = S\,, \tag{11a}$$

$$\frac{1}{\kappa_e}\left(\frac{\partial n_e u_e}{\partial t} + \nabla \cdot (n_e u_e \otimes u_e)\right) = -\frac{1}{M_e^2 \kappa_e}\Big(\nabla(n_e T_e) + n_e E\Big) - \bar{\mathcal{H}}_e\,(n_e u_e \times B) - \nu_e n_e u_e\,, \tag{11b}$$

coupled to Poisson equation

$$-\lambda^2 \Delta\phi = n_i - n_e\,, \tag{12a}$$

$$E = -\nabla\phi\,. \tag{12b}$$

Note that, for conciseness, the primes are omitted to identify the dimensionless quantities in Eqs. (10–12) and thereafter.

The hierarchy of fluid models is illustrated on Fig. 1. The bi-fluid Euler-Poisson model stands at the root of this hierarchy. This model is mainly used for the simulation of the plasma in regions of low density, predominantly in sheaths created in the vicinity of walls (see for instance [1, 2] for one dimensional non magnetized low temperature plasma simulations). One stream emerging from the root of this hierarchy is specific to quasi-neutral plasma descriptions. These models describe the evolution of the plasma with large densities on scales where

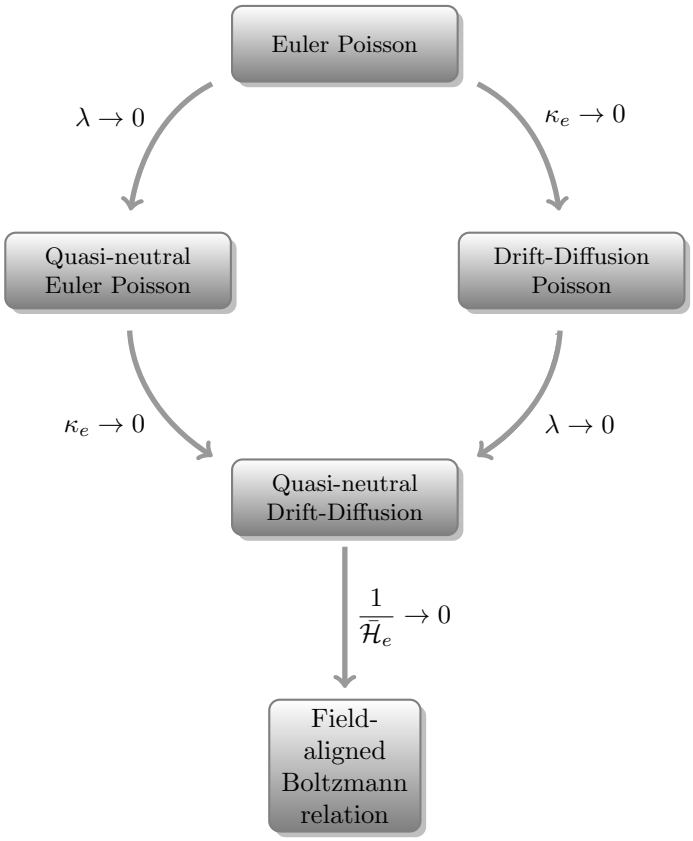

Figure 1: Hierarchy of (isothermal) fluid models.

the ions and the electrons may not be distinguished. The second stream is dedicated to plasma descriptions on the ionic time scale. These models follow the plasma bulk evolution associated to the massive ions, the fast scales attached to the electron being filtered out from the equations. Both streams are merging into a model embedding both the quasi-neutrality and the drift approximation for the electrons. Reduced models derived on these two assumptions are the most widely used for the simulation on large scales in the context of low temperature plasmas [36, 22, 1, 33, 32]. The last reduction is related to the so-called Boltzmann relation for the electrons, used very often throughout in plasma physics, in particular for low-pressure (low-collisional), non-magnetized plasmas or plasma sheaths. In the present framework, it is specific to the large magnetization of the electrons. It relies on the assumption that the electron collision frequency is small compared to cyclotron frequency. This leads to a force balance along the magnetic field lines in which the drift term, originating from the collisions with neutral, has vanished. This accounts for a departure

from the drift regime to the so-called Boltzmann relation in the direction of the magnetic field. This model is implemented in [23] for the simulation of plasma thrusters.

This hierarchy of fluid models is derived owing $\mathfrak{m} \ll 1$, the smallness of this parameter together with Eqs. (9) yields the following scaling relations

$$\frac{1}{\kappa_e} = \frac{\mathfrak{m}}{\theta}\frac{1}{\kappa_i} \ll 1\,, \qquad \frac{1}{M_e^2\kappa_e} = \frac{\theta}{\mathfrak{m}}\frac{1}{M_i^2\kappa_i} \gg 1\,, \qquad \frac{1}{\bar{\mathcal{H}}_e} = \frac{1}{\mathfrak{m}\theta}\frac{1}{\bar{\mathcal{H}}_i} \ll 1\,, \tag{13}$$

from which originates the reduced models previously mentioned and formally derived in the next sections.

2.3.2 Drift-diffusion regime for the electrons

This regime amounts to letting $M_e^2 \to 0$ but with finite values for both $(M_e^2\kappa_e)$ and $\mathcal{H}_e$. The low Mach regime of the electrons entails the assumption that collisions with neutrals are frequent $(1/\kappa_e \to 0)$. This regime prevails in the plasma bulk, where the mean velocity of the electrons roughly matches that of the ions. The low electron to ion mass ratio is therefore at the origin of the low Mach regime for the electrons (assuming $M_i^2 \sim 1$). Nonetheless, this is not representative of the dynamics developing in the entire domain. In particular, a different regime characterizes electrostatic sheaths, where the particles are accelerated by the local electric field created by the space charge, or in the acceleration region of Hall thrusters. In these regions, the flow may become supersonic [10] invalidating the low Mach regime [1, 2]. This scaling is therefore well-grounded in the core of the plasma where the evolution of the electron may be driven by the following system

$$\frac{\partial n_e}{\partial t} + \nabla\cdot(n_e u_e) = S\,, \tag{14a}$$

$$\nu_e n_e u_e + \bar{\mathcal{H}}_e\,(n_e u_e \times B) = -\frac{1}{M_e^2\kappa_e}\Big(\nabla(n_e T_e) + n_e E\Big)\,, \tag{14b}$$

The electronic velocity is provided by a mobility law, where due the magnetization of the plasma, the mobility is not a scalar but a tensor denoted $\mathbb{M}_{\mathbb{B}}$

$$u_e = -\frac{1}{M_e^2\kappa_e}\mathbb{M}_{\mathbb{B}}\left(\frac{1}{n_e}\nabla(n_e T_e) + E\right)\,, \qquad \mathbb{M}_{\mathbb{B}} = \frac{1}{\nu_e}\left(\mathbb{Id} + \mathcal{H}_e\mathbb{B}\right)^{-1}\,, \tag{15a}$$

where $\mathcal{H}_e = \nu_e\bar{\mathcal{H}}_e$, $\mathbb{Id}$ is the identity matrix and $\mathbb{B}$ the matrix verifying $\forall v \in \mathbb{R}^3$

$$\mathbb{B}v = v \times b\,, \qquad b = \frac{B}{\|B\|}\,. \tag{15b}$$

Simple algebra provides the following expression of the mobility matrix

$$\begin{aligned}\mathbb{M}_{\mathbb{B}} &= \frac{1}{\nu_e}\frac{1}{1+\mathcal{H}_e^2}\Big(\mathbb{Id} - \mathcal{H}_e\mathbb{B} + \mathcal{H}_e^2 b\otimes b\Big)\,,\\ &= \frac{1}{\nu_e}\left(\frac{1}{1+\mathcal{H}_e^2}\Big((\mathbb{Id} - b\otimes b) - \mathcal{H}_e\mathbb{B}\Big) + (b\otimes b)\right)\end{aligned} \tag{15c}$$

Note that $b\otimes b$, (resp. $\mathbb{I}\mathrm{d}-b\otimes b$) is the projector onto the direction aligned with the magnetic field (resp. onto the directions perpendicular to the magnetic field). For large values of the magnetic field $\mathcal{H}_e \gg 1$, the mobility tensor is therefore anisotropic. The aligned mobility (with respect to the magnetic field) $\mu_\parallel = \nu_e^{-1}$ ($\mu_\parallel = \mu_e$ in physical units) is large compared to the Pedersen mobility $\mu_P = \mu_\parallel/(1+\mathcal{H}_e^2) \sim \mu_\parallel/\mathcal{H}_e^2$ along the directions perpendicular to the magnetic field. The third coefficient appearing in the mobility matrix is the Hall mobility $\mu_H = \mu_\parallel \mathcal{H}_e/(1+\mathcal{H}_e^2) \sim \mu_\parallel/\mathcal{H}_e$. It is also characteristic of the dynamic in the perpendicular directions, it is indeed at the origin of the so called $E\times B$ drift. With these notations, the mobility matrix may be recast into

$$\mathbb{M}_{\mathbb{B}} = \mu_P(\mathbb{I}\mathrm{d} - b\otimes b) - \mu_H \mathbb{B} + \mu_\parallel\,(b\otimes b)\ . \tag{16}$$

In the drift regime, the electronic density is the solution of a diffusion equation. It is obtained by inserting the mobility law provided by Eqs. (15) into Eq. (14a) yielding

$$\frac{\partial n_e}{\partial t} - \frac{1}{M_e^2\kappa_e}\nabla\cdot\Big(\mathbb{M}_{\mathbb{B}}\nabla(n_eT_e)\Big) = \frac{1}{M_e^2\kappa_e}\nabla\cdot\big(\mathbb{M}_{\mathbb{B}}n_eE\big) + S\,. \tag{17}$$

The electronic system reduces to Eq. (17), the ionic properties being computed thanks to Eqs. (10). The electric field may be computed thanks to Eqs. (12), however a more elaborated equation may be derived. In this aim, integrating Eq. (17) over a (dimensionless) typical time Ξ, the following estimate can be proposed

$$n_e(t+\Xi) \approx n_e(t) + \frac{\Xi}{M_e^2\kappa_e}\Big(\mathbb{M}_{\mathbb{B}}\left(\nabla(n_eT_e) - n_e\nabla\phi\right)\Big) + \Xi S\,, \tag{18}$$

providing, thanks to Eqs. (12), the following elliptic equation satisfied by the electric protential

$$-\nabla\cdot\Big((\lambda^2 + \frac{\Xi}{M_e^2\kappa_e}n_e\mathbb{M}_{\mathbb{B}})\nabla\phi\Big) = \tilde{n}_i - \tilde{n}_e \tag{19a}$$

where

$$\begin{aligned}\tilde{n}_e &= n_e(t) + \frac{\Xi}{M_e^2\kappa_e}\left(\mathbb{M}_{\mathbb{B}}\nabla(n_eT_e)\right) + \Xi S\,,\\ \tilde{n}_i &= n_i(t) + \Xi\nabla\cdot(n_iu_i) + \Xi S\end{aligned} \tag{19b}$$

In Eq. (19), the isotropic contribution stemming from Poisson equation is carried by the squared dimensionless Debye length λ^2. The anisotropy tensor, proportional the $(M_e^2\kappa_e)^{-1}$, originates from the particle current divergence.

2.3.3 Quasi-neutral limit

The plasma may be assumed quasi-neutral when the Debye length is small compared to the typical length. This regime prevails essentially in regions of large plasma densities. It amounts to the following limit $\lambda \to 0$. In the quasi-neutral

limit, Poisson equation (8) degenerates into the balance of the electronic and ionic densities $n_e = n_i = n$. Two conclusions may be drawn from this property. First, Poisson equation is not well suited for the computation of the electric field in the quasi-neutral regime. Second, since the ionic and electronic densities are equal, one of the equations (10a) and (14a) is redundant. Classically, Eq. (10a) is used to compute the evolution of the plasma density, while the electric field is carried out thanks to the continuity equation. This latter equation provides the evolution of the charge density $\rho = n_i - n_e$, it is an outcome of both Eqs. (10a) and (14a), writing

$$\frac{\partial \rho}{\partial t} + \nabla \cdot J = 0\,, \tag{20}$$

$J = n_i u_i - n_e u_e$ being the particle current density. The quasi-neutral limit of the continuity equation (20) provides the constraint $\nabla \cdot J = 0$. In this regime, the electric field is computed to ensure a divergence free current thanks to

$$\nabla \cdot (n u_e) = S - \frac{\partial n}{\partial t} \tag{21}$$

where $n = n_e = n_i$ is the plasma density. The electric field is therefore computed thanks to equations governing the evolution of the particles properties rather than Maxwell's equations [15], hence the anisotropy of the problem. In the combined quasi-neutral and drift approximation limit, the electric field equation is indeed derived from Eqs. (19) by letting $\lambda \to 0$ yielding

$$-\nabla \cdot \Big(\mathbb{M}_{\mathbb{B}} \big(-\nabla(n T_e) + n \nabla \phi \big) \Big) = S - \frac{\partial n}{\partial t}\,. \tag{22}$$

In the standard regime, including the inertia of the electrons, the equation providing the electric potential is derived from Eqs. (11). We refer, for instance to [18] for such a derivation.

2.3.4 Field aligned Boltzmann relation

This last asymptotic consists in assuming an infinite anisotropy, letting $1/\mathcal{H}_e \to 0$. The mobility relation defined by Eqs. (15) leads to the following force balance

$$b \cdot \nabla(n T_e) - n b \cdot \nabla \phi = 0\,. \tag{23}$$

To provide a finite electronic velocity along the magnetic field lines, a zero force balance is mandatory along this direction. Note that, owing to the homogeneous electronic temperature, this force derives from the potential ψ defined as

$$\psi = -\phi + T_e \ln\left(\frac{n}{n_0}\right) \tag{24}$$

n_0 being a reference of the density. Denoting $\mathcal{F} = \nabla \psi$ the force field, the equilibrium stated by Eq. (23) amounts to a zero force regime along the magnetic field lines

$$b \cdot \mathcal{F} = 0\,. \tag{25}$$

To outline the characteristics of this regime in a simple framework, the magnetic field is assumed constant and aligned with the z-coordinate. The force balance occurring along the magnetic field lines simplifies into

$$\frac{\partial \phi}{\partial z} = \frac{T_e}{n_e} \frac{\partial n_e}{\partial z} \,. \tag{26}$$

Classically, this differential equation is integrated to provide the so-called Boltzmann relation

$$n_e(x,y,z) = n_0(x,y) \exp\left(\frac{\phi(x,y,z) - \phi_0(x,y)}{T_e(x,y)} \right) , \tag{27}$$

where n_0, ϕ_0 and T_e are independent of the aligned coordinate z. Combined with Poisson equation, it provides a non linear equation satisfied by the electric potential

$$-\lambda \Delta \phi = n_i - n_0 \exp\left(\frac{\phi}{T_e} \right) . \tag{28}$$

Note that this non linear equation is not degenerate in the quasi-neutral limit [18]. In the context of quasi-neutral plasma modelling, Eq. (27) is used to compute the electric potential thanks to the density with

$$\phi(x,y,z) = \phi_0(x,y) + T_e(x,y) \ln\left(\frac{n(x,y,z)}{n_0(x,y)} \right) , \tag{29}$$

In the literature [23, 38], this identity is sometimes referred to as the Morozov approximation [34]. This equation is coupled with the ionic system (10) to close the system providing the evolution of the plasma density.

3 Numerical methods for quasi-neutral fluid models of magnetically confined low temperature plasmas.

3.1 Model and geometrical configuration

The purpose here is to state the complete set of equations operated to illustrate the difficulty raised by quasi-neutral modelling of plasma thrusters. The computations are restricted to two dimensional configurations, in a plane containing both the electric and the magnetic field. The system defining the model is specified in dimensional units. Let n be the plasma density, v the ionic mean velocity and Γ_e the electronic density flux, these equations write

$$\frac{\partial n}{\partial t} + \nabla \cdot (nv) = S \,, \qquad \text{in } (0,\infty) \times \Omega \,, \tag{30a}$$

$$\frac{\partial}{\partial t}(nv) + \nabla \cdot (nv \otimes v) = \frac{e}{m_i} nE \,, \qquad \text{in } (0,\infty) \times \Omega \,, \tag{30b}$$

$$\nabla \cdot \Gamma_e = S - \frac{\partial n}{\partial t} \qquad \text{in } \Omega \,, \tag{30c}$$

with

$$\Gamma_e = \mu_e\big(n\nabla_\parallel\phi - \nabla_\parallel(nk_BT_e)\big) + \mu_e\varepsilon\big(n\nabla_\perp\phi - \nabla_\perp(nk_BT_e)\big)\,, \tag{30d}$$

the electrostatic field and potential satisfying the following identity $E = -\nabla\phi$. Note that, owing to the geometrical configuration, the Hall components in the mobility law defined by Eq. (16) are dropped out of these equations, hence the definition of the electronic density flux as a function of the only parallel mobility $\mu_\parallel = \mu_e = em_e/\nu_e$, ν_e being the collision frequency against neutral, and the Perdersen mobility $\mu_P = \mu_e\varepsilon$. The anisotropic parameter ε is related to the electronic Hall parameter $\mathcal{H}_e$ thanks to

$$\varepsilon = \frac{1}{1+\mathcal{H}_e^2}\,, \qquad \mathcal{H}_e = \mu_e\|B\| = \frac{\omega_{c,e}}{\nu_e}\,. \tag{30e}$$

The source term in Eq. (30a) accounts for the ionization. The following expression will be considered in Sec. 4.2

$$S(x,y) = \nu n_0 \exp\big(-(\tau y)^2\big)\,, \tag{30f}$$

where ν is the ionization frequency n_0 the typical plasma density and $\tau > 0$ parametrizes the distribution of the neutral density in the domain. The parallel and perpendicular gradients are defined for any smooth function ψ as

$$\nabla_\parallel\psi = b\otimes b\nabla\psi\,, \qquad \nabla_\perp\psi = (\mathbb{I}\mathrm{d} - b\otimes b)\nabla\psi\,, \qquad b = \frac{B}{\|B\|}\,. \tag{30g}$$

The computational domain, denoted $\Omega\times[0,T]$, consists of $\Omega = [0,Lx]\times[-L_y/2, L_y/2]$ where L_x and L_y are positive real numbers. The domain boundary is split into two parts $\partial\Omega_x = [0,L_x]\times\{-L_y/2, L_y/2\}$ and $\partial\Omega_y = \{0,L_x\}\times[-L_y/2, L_y/2]$, the following boundary conditions supplementing the system (30)

$$\nabla n\cdot\boldsymbol{n} = 0 \qquad \text{on } (0,T)\times\partial\Omega_y\,, \tag{31a}$$
$$\nabla(nv)\boldsymbol{n}\cdot\boldsymbol{n} = 0 \qquad \text{on } (0,T)\times\partial\Omega_x\,, \tag{31b}$$
$$v\cdot\boldsymbol{n} = 0 \qquad \text{on } (0,T)\times\partial\Omega_y\,, \tag{31c}$$
$$v\cdot\boldsymbol{n} = v_B \qquad \text{on } (0,T)\times\partial\Omega_x\,, \tag{31d}$$
$$\Gamma_e\cdot\boldsymbol{n} = 0 \qquad \text{on } \partial\Omega_y\,, \tag{31e}$$
$$\Gamma_e\cdot\boldsymbol{n} = \Gamma_\beta(\phi) \qquad \text{on } \partial\Omega_x\,. \tag{31f}$$

The domain outward normal is denoted $\boldsymbol{n}$, v_B is the Bohm velocity

$$v_B^2 = \frac{k_BT_e}{m_i}\,. \tag{31g}$$

Specifying the boundary condition of the quasi-neutral model to account the physics that develops on the sheath edge is an intricate issue. We propose and investigate here the following path. On the one hand, the electrons are assumed to flow outside the domain along the magnetic field lines with the most probable

velocity computed from the local Maxwellian distribution ($\sqrt{k_B T_e/2\pi m_e}$). On the other hand, when the magnetic field is parallel to the boundary, the electron flux is assumed to match that of the ions. Denoting β the angle measured between the magnetic field and $\boldsymbol{n}$ the outward normal on $\partial\Omega_x$, the following boundary condition is therefore considered

$$\Gamma_\beta(\phi) = n\sqrt{\frac{k_B T_e}{2\pi m_e}\cos^2(\beta) + v_B^2 \sin^2(\beta)}\exp\left(-\frac{e\phi}{k_B T_e}\right). \tag{31h}$$

The initial condition is prescribed thanks to

$$n(t=0) = n_0\,, \qquad v(t=0) = v_0\,, \qquad \text{on } \Omega\,. \tag{32}$$

In this model, the electric potential is used to enforce the quasi-neutrality constraint (30c). It yields the following non-linear anisotropic problem for ϕ

$$\begin{aligned}
&-\nabla\cdot\left(\mu n\nabla_\parallel\psi + \mu n\varepsilon\nabla_\perp\psi\right) = S - \frac{\partial n}{\partial t} && \text{in } \Omega, && (33a)\\
&\left(\mu n\nabla_\parallel\psi + \mu n\varepsilon\nabla_\perp\psi\right)\cdot\boldsymbol{n} = 0 && \text{on } \partial\Omega_y, && (33b)\\
&\left(\mu n\nabla_\parallel\psi + \mu n\varepsilon\nabla_\perp\psi\right)\cdot\boldsymbol{n} = \Gamma_\beta\left(-\psi + \frac{k_B T_e}{e}\ln\left(\frac{n}{n_0}\right)\right) && \text{on } \partial\Omega_x, && (33c)
\end{aligned}$$

where

$$\psi = -\phi + \frac{k_B T_e}{e}\ln\left(\frac{n}{n_0}\right). \tag{33d}$$

The non linearity of the problem stems from the boundary condition (33c). This problem is approximated by a sequence of linearised problems providing the solution estimates $(\psi^{(k)})_{k\geq 0}$ thanks to

$$\begin{aligned}
&-\nabla\cdot\left(\mu n\nabla_\parallel\psi^{(k+1)} + \mu n\varepsilon\nabla_\perp\psi^{(k+1)}\right) = S - \frac{\partial n}{\partial t} && \text{in } \Omega, && (34a)\\
&\left(\mu n\nabla_\parallel\psi^{(k+1)} + \mu n\varepsilon\nabla_\perp\psi^{(k+1)}\right)\cdot\boldsymbol{n} = 0 && \text{on } \partial\Omega_y, && (34b)\\
&\left(\mu n\nabla_\parallel\psi^{(k+1)} + \mu n\varepsilon\nabla_\perp\psi^{(k+1)}\right)\cdot\boldsymbol{n} = \\
&\qquad -\Gamma'_\beta\left(-\psi^{(k)} + \frac{k_B T_e}{e}\ln\left(\frac{n}{n_0}\right)\right)\left(\psi^{(k+1)} - \psi^{(k)}\right) && \text{on } \partial\Omega_x, && (34c)
\end{aligned}$$

where Γ'_β is the derivative of Γ_β, obeying the relationship

$$\Gamma'_\beta(\varphi) = -\frac{e}{k_B T_e}\Gamma_\beta(\varphi)\,. \tag{34d}$$

3.2 Handling numerically the anisotropy

The difficulty raised by the anisotropic nature of the problem is analyzed in this section. To support these investigations, the system (34) is simplified, assuming

$\mu n = 1$ and $\Gamma'_\beta \equiv 0$, yielding the following toy problem

$$
\begin{aligned}
&-\Delta_\perp \psi - \frac{1}{\varepsilon}\Delta_\parallel \psi = f\,, && \text{in } \Omega && \text{(35a)}\\
&\left(\varepsilon \nabla_\perp \psi + \nabla_\parallel \psi\right)\cdot \boldsymbol{n} = 0\,, && \text{on } \partial\Omega_N\,, && \text{(35b)}\\
&\psi = 0 && \text{on } \partial\Omega_D && \text{(35c)}
\end{aligned}
$$

with

$$
\begin{aligned}
&\partial\Omega_N = \{\boldsymbol{x} \in \partial\Omega,\, b(\boldsymbol{x})\cdot \boldsymbol{n}(\boldsymbol{x}) \neq 0\}\,, \qquad \partial\Omega_D = \partial\Omega \setminus \partial\Omega_N\,, && \text{(35d)}\\
&\Delta_\parallel \psi = \nabla\cdot\nabla_\parallel \psi\,, \qquad \Delta_\perp \psi = \nabla\cdot\nabla_\perp \psi\,. && \text{(35e)}
\end{aligned}
$$

Let, p be the precision order on the numerical schemes at hand to carry out the approximation of the differential operators (with respect to the coordinates), the following estimates hold true:

$$
(\Delta^h_\parallel \Psi^h)_{i,j} = \Delta_\parallel \psi(x_i, y_j) + \mathcal{O}_\parallel(h^p)\,, \quad (\Delta^h_\perp \Psi^h)_{i,j} = \Delta_\perp \psi(x_i, y_j) + \mathcal{O}_\perp(h^p)\,.
$$

The discrete operators are denoted $\Delta^h_\parallel$ and $\Delta^h_\perp$, Ψ^h is the discrete approximation of the solution, the mesh being defined by the node positions (x_i, y_j) and the typical mesh size h. The truncation errors $\mathcal{O}_\parallel(h^p)$ and $\mathcal{O}_\perp(h^p)$ are functions of the mesh size and the derivatives of the solution and magnetic field with respect to x and y. This yields the following scheme:

$$
-(\Delta^h_\perp \Psi^h)_{i,j} - \frac{1}{\varepsilon}(\Delta^h_\parallel \Psi^h)_{i,j} = f^h_{i,j} - \mathcal{O}_\perp(h^p) - \frac{1}{\varepsilon}\mathcal{O}_\parallel(h^p) \tag{36}
$$

This unravels an amplification of the truncation error $\mathcal{O}_\parallel(h^p)$ issued from parallel operator discretizarion by $1/\varepsilon$. A deterioration of the numerical method precision with decreasing ε-values can therefore be anticipated, precisely a linear growth of the error with ε^{-1}, eventually leading to ineffective computations for large anisotropies. We refer to Sec. 4.1 for numerical investigations illustrating this feature and to [41] for a thorough analysis of this issue.

A workaround consists in working a "rescaled" variable harnessed to cancel this amplification of the truncation error, owing to the property $\nabla_\parallel q = \varepsilon^{-1}\nabla_\parallel \psi$. The re-scaled variable may be computed thanks to ψ by substituting $\varepsilon^{-1}\nabla_\parallel \psi$ by $\nabla_\parallel q$ in Eqs. (35). This provides

$$
\begin{aligned}
&-\Delta_\parallel q = f + \Delta_\perp \psi\,, && \text{in } \Omega\\
&\nabla_\parallel q \cdot \boldsymbol{n} = -\nabla_\perp \psi \cdot \boldsymbol{n}\,, && \text{on } \partial\Omega_N\,,
\end{aligned}
$$

This system is not well posed for q, since the solution of this problem can be augmented by any function with no parallel gradient. Uniqueness may be restored in this system by imposing the value of q on every field line. Let $\partial\Omega_0$ be the subset of Ω onto which the condition $q = 0$ is imposed to restore the well posedness of the problem. The definition of $\partial\Omega_0$ is specific to the magnetic field geometry and will be specified in the sequel. This condition is introduced

into the system by means of a Lagrange multiplier. This yields the following set of equations to compute the re-scaled variable q together with the Lagrange multiplier $\mathscr{L}$ defined on $\partial\Omega_0$ ($\mathscr{L} \equiv 0$ on $\Omega/\partial\Omega_0$)

$$
\begin{aligned}
-\Delta_{\parallel} q + \mathscr{L} &= f + \Delta_{\perp}\psi && \text{in } \Omega && (38a)\\
\nabla_{\parallel} q \cdot \boldsymbol{n} &= -\nabla_{\perp}\psi \cdot \boldsymbol{n} && \text{on } \partial\Omega_N\,, && (38b)\\
q &= 0 && \text{on } \partial\Omega_0 && (38c)
\end{aligned}
$$

This problem is coupled with

$$
\begin{aligned}
-\Delta_{\parallel}\psi &= -\varepsilon\Delta_{\parallel} q && \text{in } \Omega && (38d)\\
\nabla_{\parallel}\psi \cdot \boldsymbol{n} &= -\varepsilon\nabla_{\parallel} q \cdot \boldsymbol{n} && \text{on } \partial\Omega_N\,, && (38e)\\
\psi &= 0 && \text{on } \partial\Omega_D\,, && (38f)
\end{aligned}
$$

to define a set of equations providing $(\psi, q, \mathscr{L})$ and referred to as the augmented Micro-Macro system. The merits of the re-scaled system defined by Eqs. (38) are outlined thanks to a discretization of Eq. (38d)

$$
-\left(\Delta_{\parallel}^h \Psi^h\right)_{i,j} = -\varepsilon\left(\Delta_{\parallel}^h Q^h\right)_{i,j} + \mathcal{O}_{\parallel,\psi}(h^p) + \varepsilon\mathcal{O}_{\parallel,q}(h^p)\,, \tag{39}
$$

In this equation Q^h is the numerical approximation of q, $\mathcal{O}_{\parallel,\psi}(h^p)$ and $\mathcal{O}_{\parallel,q}(h^p)$ are the truncation errors stemming from the discretization of $\Delta_{\parallel}\psi$ and $\Delta_{\parallel} q$. For intense anisotropies, the contribution of Q^h in this equation is masked by the truncation error: $\varepsilon\mathcal{O}_{\parallel,q}(h^p) \ll \mathcal{O}_{\parallel,\psi}(h^p)$. Eq. (39) accounts for the property $-\Delta\psi = 0$, satisfied by the solution in the limit $\varepsilon \to 0$, but with the precision of the numerical scheme $\mathcal{O}(h^p)$. Finally, note that Eqs. (38a-38c) are independent of the anisotropy, therefore any discretization provides a numerical method free from an error amplification when $\varepsilon \to 0$.

The augmented Micro-Macro method will be compared to the classical "Inflow" method which consists of the following set of equations

$$
\begin{aligned}
-\Delta_{\perp}\psi - \Delta_{\parallel} q &= f && \text{in } \Omega && (40a)\\
-\Delta_{\parallel}\psi &= -\varepsilon\Delta_{\parallel} q && \text{in } \Omega && (40b)\\
\nabla_{\parallel} q \cdot \boldsymbol{n} &= -\nabla_{\perp}\psi \cdot \boldsymbol{n} && \text{on } \partial\Omega_N\backslash\partial\Omega_0\,, && (40c)\\
\nabla_{\parallel}\psi \cdot \boldsymbol{n} &= -\varepsilon\nabla_{\parallel} q \cdot \boldsymbol{n} && \text{on } \partial\Omega_N\,, && (40d)\\
\psi &= 0 && \text{on } \partial\Omega_D\,, && (40e)\\
q &= 0 && \text{on } \partial\Omega_0 && (40f)
\end{aligned}
$$

where $\partial\Omega_0$ is a subset of $\partial\Omega_N$ with

$$
\partial\Omega_0 = \{\boldsymbol{x} \in \partial\Omega_N, b(\boldsymbol{x}) \cdot \boldsymbol{n}(\boldsymbol{x}) > 0\}\,. \tag{40g}
$$

In the Inflow MM method, the boundary condition for q on one part of $\partial\Omega_N$ is substituted by a zero condition yielding to Eqs. (40c) and (40f). No Lagrange multiplier is therefore used to impose the value of q on every field line in this method.

A similar augmented Micro-Macro (a-MM) system is stated for the linearised problem (34), yielding

$$-\nabla\cdot\Big(\mu n\varepsilon\nabla_{\parallel}q^{(k+1)}+\mu n\varepsilon\nabla_{\perp}\psi^{(k+1)}\Big)+\mathscr{L}^{(k+1)}=S-\frac{\partial n}{\partial t}\qquad\text{in }\Omega,\qquad(41a)$$

$$-\nabla\cdot\Big(\mu n\varepsilon\nabla_{\parallel}q^{(k+1)}-\mu n\nabla_{\parallel}\psi^{(k+1)}\Big)=0\qquad\text{in }\Omega,\qquad(41b)$$

$$\Big(\mu n\varepsilon\nabla_{\parallel}q^{(k+1)}+\mu n\varepsilon\nabla_{\perp}\psi^{(k+1)}\Big)\cdot\boldsymbol{n}=0\qquad\text{on }\partial\Omega_y,\qquad(41c)$$

$$q^{(k+1)}=0\qquad\text{on }\partial\Omega_y,\qquad(41d)$$

$$\Big(\mu n\varepsilon\nabla_{\parallel}q^{(k+1)}+\mu n\varepsilon\nabla_{\perp}\psi^{(k+1)}\Big)\cdot\boldsymbol{n}=-\Gamma'_{\beta}\left(-\psi^{(k+1)}+\frac{k_BT_e}{e}\ln\left(\frac{n}{n_0}\right)\right)\Big(\psi^{(k+1)}-\psi^{(k)}\Big)\qquad\text{on }\partial\Omega_x,\qquad(41e)$$

$$\Big(\mu n\varepsilon\nabla_{\parallel}q^{(k+1)}-\mu n\nabla_{\parallel}\psi^{(k+1)}\Big)\cdot\boldsymbol{n}=0\qquad\text{on }\partial\Omega_x,\qquad(41f)$$

$$q^{(k+1)}=0\qquad\text{on }\partial\Omega_0\qquad(41g)$$

4 Demonstrative calculations

4.1 Validation of the augmented Micro-Macro method

In this section, the capability of the elliptic problem solver to recover a precise approximation of the force field and potential ($\mathcal{F}$ and ψ), irrespective to the anisotropy strength, is examined. In this aim, a manufactured solution of the toy model defined by Eqs. (35) is therefore proposed. This simplified set-up enables to carry out analytically the computations, providing an exact reference solution to validate the numerical methods mobilized for the resolution of the anisotropic problem. The computational domain is $\Omega=[0,1]^2$, the magnetic field is provided by the following equations

$$B_x(x,y)=\pi\aleph\zeta(x^2-x)\sin(\aleph\pi y)\,,\quad B_y(x,y)=\zeta\,(2x-1)\cos(\aleph\pi y)+\pi\,.\qquad(42a)$$

The manufactured solution for the potential, denoted ψ_{m}, is defined by means of two components ψ_0 and ψ_1 with

$$\begin{aligned}\psi_{\mathrm{m}}(x,y)&=\psi_0(x,y)+\varepsilon\psi_1(x,y)\,,\\&=\sin\Big(k\big(\pi x+\zeta(x^2-x)\cos(\aleph\pi y)\big)\Big)+\varepsilon\Big(\cos(2\pi y)\sin(\pi x)\Big)\,.\end{aligned}\qquad(42b)$$

The curvature of the magnetic field is parametrized by $\zeta\in\mathbb{R}$, $\zeta\geq 0$. The second parameter, $k\in\mathbb{N}$, provides a control of the perpendicular gradient of the solution in the limit $\varepsilon\to 0$, the variations of the solution perpendicular to the magnetic field being reduced to that of ψ_0 for large anisotropy strengths. The set-up associated to the manufactured solution is illustrated on the plots of Fig. 2. The auxiliary variable is set to zero along an horizontal line intersecting any field line, at the bottom ($y=0$ or the top $y=1$) of the computational domain. This amounts to the definition $\partial\Omega_0=\{(x,y)\in]0,1[\times\{0\}\}$.

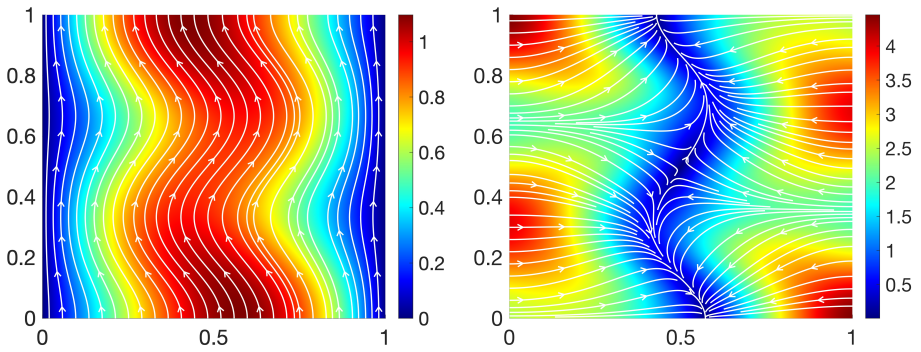

(a) $\zeta = 1$, $k = 1$, $\varepsilon = 10^{-1}$.

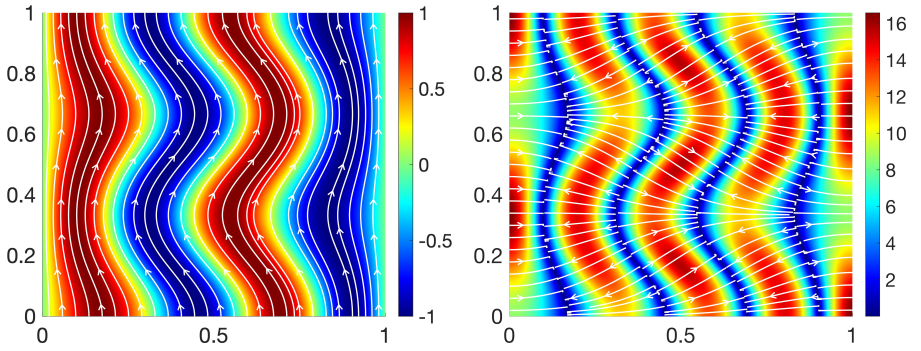

(b) $\zeta = 1$, $k = 4$, $\varepsilon = 10^{-6}$.

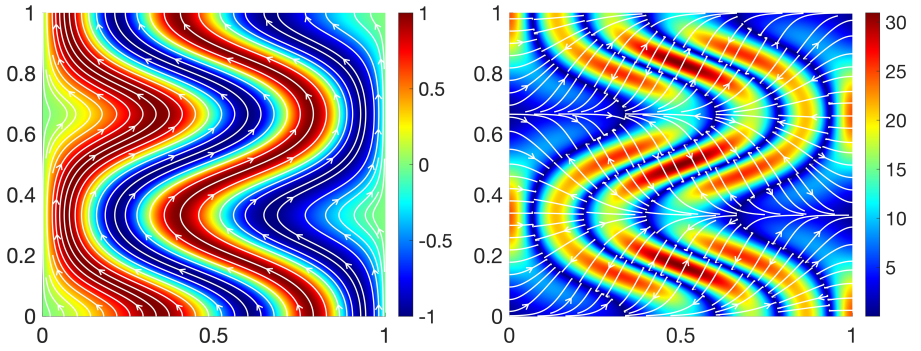

(c) $\zeta = 3$, $k = 4$, $\varepsilon = 10^{-6}$.

Figure 2: Manufactured solution defined by Eqs. (42): Magnetic field lines and potential values (ψ) in a color scale (left); force field ($\mathcal{F}$) lines and magnitude $\|\mathcal{F}\|_2$ in a color scale (right) for $\aleph = 3$.

The precision of the numerical method is not experienced to depend significantly on the choice of $\partial\Omega_0$. The plots of Fig. 3a and 3b are related to the

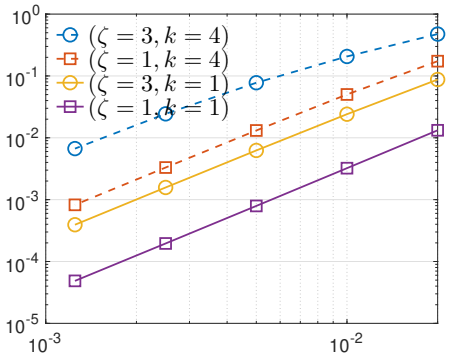

(a) (a-MM): $\|\Psi^h - \psi_{\mathrm{m}}\|_\infty / \|\psi_{\mathrm{m}}\|_\infty$, $\varepsilon = 10^{-1}$.

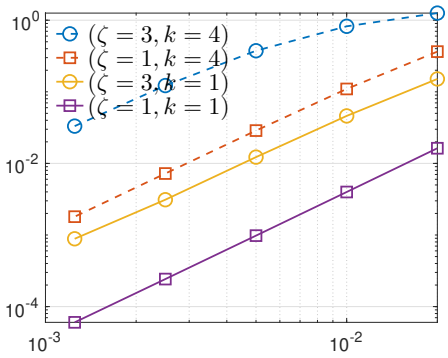

(b) (a-MM): $\|\Psi^h - \psi_{\mathrm{m}}\|_\infty / \|\psi_{\mathrm{m}}\|_\infty$, $\varepsilon \leq 10^{-6}$.

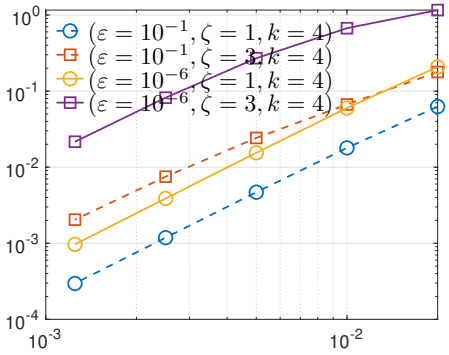

(c) (a-MM): $\|\boldsymbol{\mathcal{F}}^h - \mathcal{F}_{\mathrm{m}}\|_2 / \|\mathcal{F}_{\mathrm{m}}\|_2$.

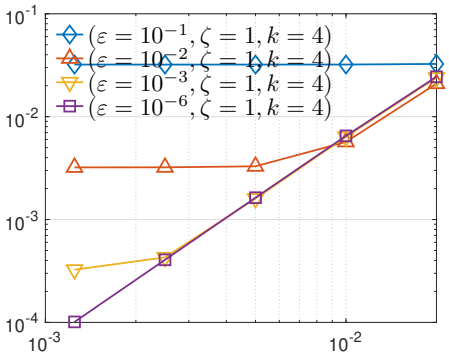

(d) (a-MM): $\|b \cdot \boldsymbol{\mathcal{F}}^h\|_2 / \|\mathcal{F}_{\mathrm{m}}\|_2$.

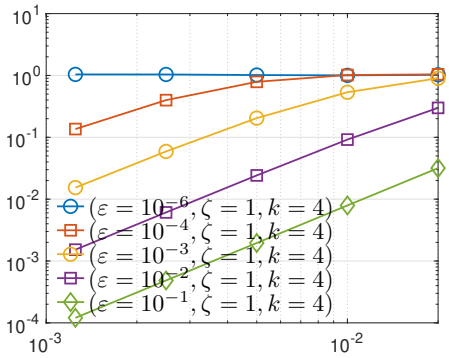

(e) (FD): $\|\Psi^h - \psi_{\mathrm{m}}\|_\infty / \|\psi_{\mathrm{m}}\|_\infty$.

Figure 3: Manufactured solution: Relative error norms for the potential Ψ^h and force field $\boldsymbol{\mathcal{F}}^h$ carried out by either a finite difference (FD) or the augmented Micro-Macro (a-MM) scheme as functions of the mesh size ($\aleph = 3$).

accuracy of Ψ^h the potential numerical approximation. The precision of the augmented Micro-Macro method (a-MM) is observed to be effective and hardly altered by ε-values. The same conclusions may be drawn from the approxima-

tion of the force field $\mathcal{F} = \nabla\psi$ plotted on Fig. 3c. Finally, the property to recover the orthogonality of the magnetic and force fields is investigated thanks to Fig. 3d. The deviation from the orthogonality is proportional to ε (precisely $\varepsilon b \cdot \nabla\psi_1 = b \cdot \nabla\psi_{\mathrm{m}}$). This is what the numerical approximation reproduces as long as the precision of the discretization is sufficient. Indeed, the plots of Fig. 3c confirm the estimate $\|\boldsymbol{\mathcal{F}}^h - \nabla\psi_{\mathrm{m}}\|_2 = \mathcal{O}(h^p)$, h denoting the typical mesh size and p the approximation order ($p = 2$ for these computations). It follows that $\|b \cdot \boldsymbol{\mathcal{F}}^h\|_2 = \mathcal{O}(\varepsilon) + \mathcal{O}(h^p)$. This estimate is in line with the plateau observed on the plots of Fig. 3d related to computations carried out with refined meshes and moderate anisotropy strengths ($\varepsilon \geq 10^{-3}$). These plateaus account for an orthogonality default dominating the approximation error ($\mathcal{O}(\varepsilon) \geq \mathcal{O}(h^p)$). Conversely, for $\varepsilon < 10^{-4}$, the numerical method is not precise enough, the deviation from the orthogonality is hidden by the discretization error.

The picture is very different for approximations computed thanks to a discretization of the anisotropic problem using finite differences (FD), as displayed on Fig. 3e. The amplification of the truncation error by ε^{-1} is clearly illustrated on these error plots: the same convergence rate is observed for $\varepsilon = 10^{-1}$ and $\varepsilon = 10^{-2}$ (eventually for $\varepsilon = 10^{-3} - 10^{-4}$ and refined meshes), however, the error value is increased by one order of magnitude when ε is decreased by 10. The precision of this method obeys the following estimate $\|\Psi^h - \psi_m\|_2 = \mathcal{O}(h^p \cdot \varepsilon^{-1})$, in line with Eq. (36). This prevents the computation of an effective numerical approximation for intense anisotropy.

4.2 Plasma confinement in a cusp-shaped magnetic field

4.2.1 Assessment of the numerical model to reproduce the physics of plasma thruster

The purpose here is to provide representative simulations of the physics involved in plasma thruster operating. Simulating the whole device is far beyond the scope of the present work, the model at hand is too coarse for such an ambitious goal. However, we aim to produce meaningful simulations of plasma confinement and prove that the numerical method developed within this paper is efficient to carry out simulations with parameters (anisotropies) representative of plasma thrusters. Specifically, the plasma confinement by a cusp-shaped magnetic field [37, 25] is investigated. This is quite challenging for numerical methods. In part due to the singularity of the magnetic field, or more precisely that of the normalized magnetic field, the magnetic field vanishing locally (in space). More importantly, due to the significant curvature of the magnetic field lines. Finally, this is also due to the concentration of magnetic field lines in punctual regions of the simulation domain. The specific application targeted here is indeed related

to a cusp shaped magnetic field [31] $B = (B_x, B_y)$ defined as

$$B_x(x,y) = -\sqrt{\gamma}\sin\left(\frac{2\pi x}{L_x}\right)\Big(\exp\left(-\pi y_-\right) - \exp\left(-\pi y_+\right)\Big), \tag{43a}$$

$$B_y(x,y) = \sqrt{\gamma}\cos\left(\frac{2\pi x}{L_x}\right)\Big(\exp\left(-\pi y_-\right) + \exp\left(-\pi y_+\right)\Big), \tag{43b}$$

$$y_- = \frac{L_y - 2y}{L_y}\,, \qquad y_+ = \frac{L_y + 2y}{L_y} \tag{43c}$$

and plotted on Fig. 4a. The magnitude of the magnetic field is parameterized by $\gamma > 0$. The model defined by Eqs. (30-33) is discretized thanks to the methods detailed in Appendix A. Note that these discretizations are quite standard, the difficulty being addressed algebraically, thanks to the introduction of the re-scaled variable into the linearized system (41). The numerical investigations are performed on a square domain with $L_x = L_y = 0.1$ m. A plasma of Argon is considered, with a typical density $n_0 = 10^{18}$ m^{-3} and an ionic mass $m_i = 6.69\,10^{-26}$ kg, the electronic temperature and mobility being set to $T_e = 11604$ K (1 eV), $\mu_e = 10^4$ T^{-1}. The magnetic field amplitude is $B_0 = 10^{-1}$ T yielding a typical Hall parameter $\mathcal{H}_e = 10^3$, at the plasma edge, this value being much weaker in the center. The initial data consists of $n(x,y,t=0) = n_0 = 10^{18}$ m^{-3}, $v(x,y,t=0) = 2v_B y/L_y$ m $\cdot$ s^{-1}, $v_B = \sqrt{k_B T_e/m_i} = 1.55\,10^3$ m $\cdot$ s^{-1} being the Bohm velocity. Note that, with this value of the Hall parameter, the ratio between the parallel and the perpendicular mobilities, is as large as 10^6 near the vessel walls, as depicted on the plot of Fig. 4b. The plasma creation in the inter-electrode chamber is accounted for by the source term in Eq. (30f) with $\nu = 1.55\,10^3$ s^{-1} and $\tau = 1.3\,10^2$ m^{-1}. The ionization is predominant in the centre of the inter electrode region as illustrated on Fig. 4c.

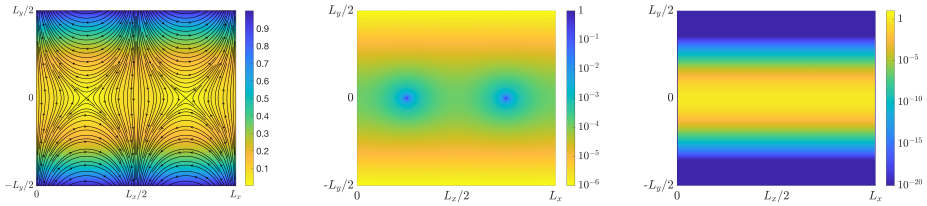

(a) Field lines and amplitude of B (Eqs. (43)) for $\gamma = 1$.

(b) Anisotropic parameter ε (Eq. (30e)) for $\|\mathcal{H}_e\|_\infty = 10^3$.

(c) Ionisation term S.

Figure 4: Set-up for plasma confinement by a cusp-shaped magnetic field.

The purpose here, is to capture the steady state of the system. The plasma characteristics remain unchanged when the loss of particles along the electrodes is matched by the ionisation in the inter-electrodes region. The computations are carried out on a mesh with 399×399 nodes to avoid the singularity of the

magnetic field in $\{L_x/4, 3L_x/4\} \times \{0\}$. The steady state defines a regime very similar to the one investigated in the previous section: in the regions of large anisotropies (near the electrodes), the source term in Eq. (33a) is vanishing, therefore, the solution may develop parallel and perpendicular gradients with very disparate magnitudes. This is confirmed by the plot of ψ the solution of the anisotropic problem as displayed on Fig. 5. This variable is almost constant

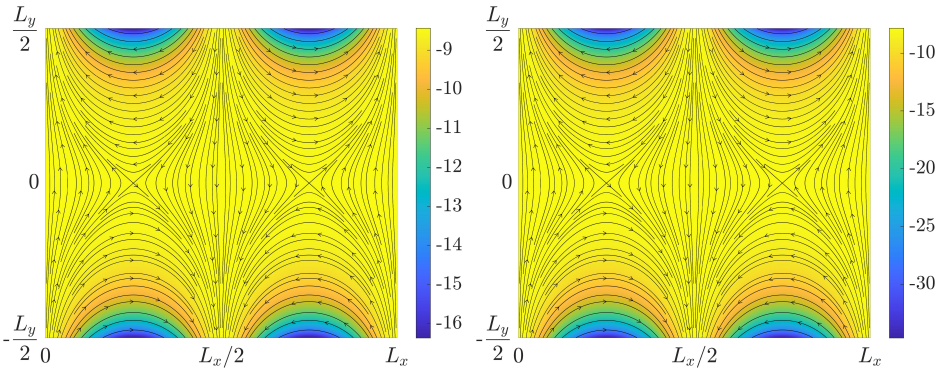

(a) $\|\mathcal{H}_e\|_\infty = 3 \cdot 10^2$. (b) $\|\mathcal{H}_e\|_\infty = 10^3$.

Figure 5: Solution of the anisotropic problem ψ ($\mathrm{V} \cdot \mathrm{m}^{-1}$) in a color scale and magnetic field lines carried out with different intensities of magnetic field.

along the magnetic field lines near the electrodes while the variations perpendicular to the magnetic field are large. The confinement of the plasma is manifest on the plot of the density obtained at the steady state (see Fig. 6). For small magnetization intensity ($\|\mathcal{H}_e\|_\infty = 10$, see Fig. 6a) the density created in the middle of the inter-electrode region is almost uniformly transported towards the electrodes as depicted by the plot of Fig 7a. With the increase of the magnetic field intensity, quasi-vacuum basins are formed along the electrodes, centred at $x = \{L_x/4, 3L_x/4\}$ in between the cusps of the magnetic field, as depicted on the plots of Figs. 6b–6d. The regions that are not connected to the middle of the inter-electrode chamber by the magnetic field lines, where the ionization is the most effective, are drained from particles. The inflow of particles from the center of the chamber, where the ionization is the most effective, into these basins is attenuated by the magnetization: the density decreases below 10^6 m^{-3} for $\mathcal{H}_e = 10^3$ while it remains larger to 10^{12} m^{-3} for $\mathcal{H}_e = 3\,10^2$. This is explained by the mitigation of the transport perpendicular to the magnetic field with the increase of the field intensity. The plots of the electronic flux (Fig. 7) show that the electrons are deflected in regions where the magnetic field lines are converging. The ions are accelerated by the electric field (see Fig. 8) towards the same regions as displayed by the plots of Fig. 9.

The confinement of the plasma may be assessed by the space integral of the particle number density over the computational domain at the steady state. This quantity is plotted on Fig. 10. Note that these computations are carried

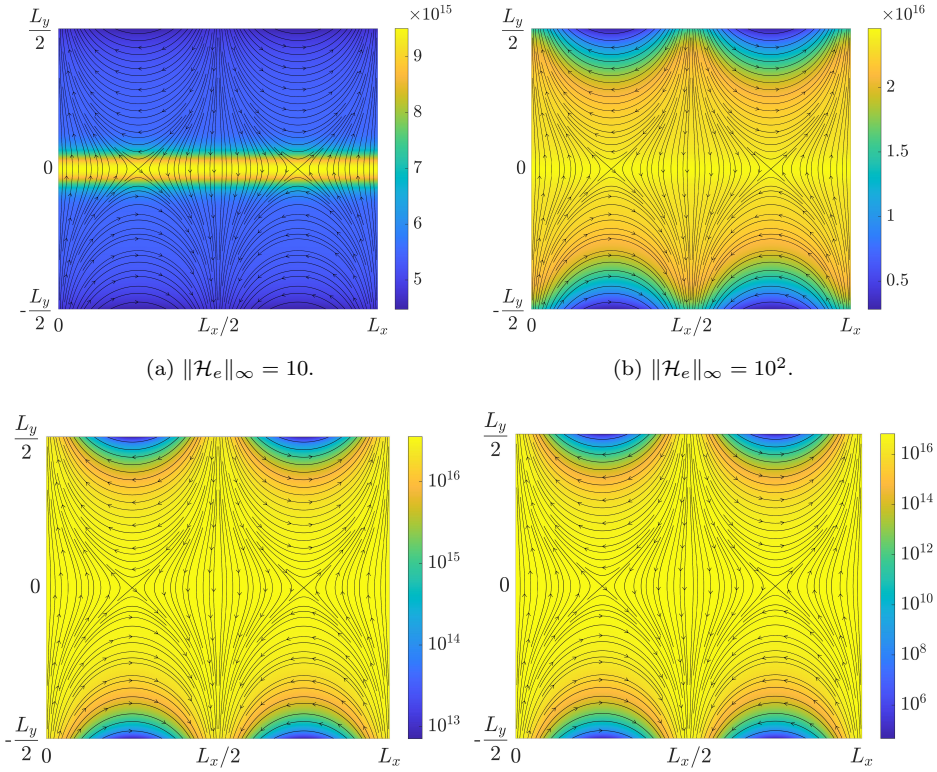

(a) $\|\mathcal{H}_e\|_\infty = 10$. (b) $\|\mathcal{H}_e\|_\infty = 10^2$.

(c) $\|\mathcal{H}_e\|_\infty = 3 \cdot 10^2$ (log. scale). (d) $\|\mathcal{H}_e\|_\infty = 10^3$ (log. scale).

Figure 6: Plasma density (in a logarithmic color scale for subplots (c) and (d)) and magnetic field lines carried out with different intensities of magnetic field.

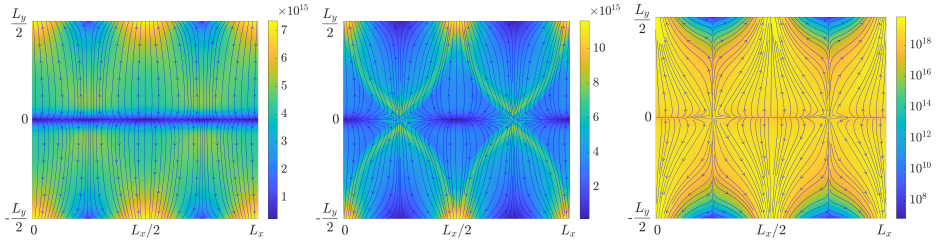

(a) $\|\mathcal{H}_e\|_\infty = 10$. (b) $\|\mathcal{H}_e\|_\infty = 10^2$. (c) $\|\mathcal{H}_e\|_\infty = 10^3$ (log. scale).

Figure 7: Electronic flux density $\Gamma_e = nu_e$ ($\mathrm{m}^{-2}\cdot\mathrm{s}^{-1}$) for different magnetisation intensities.

out with the same source term but different values of the Hall parameter. The total number of particles is observed to increase with the Hall parameter which

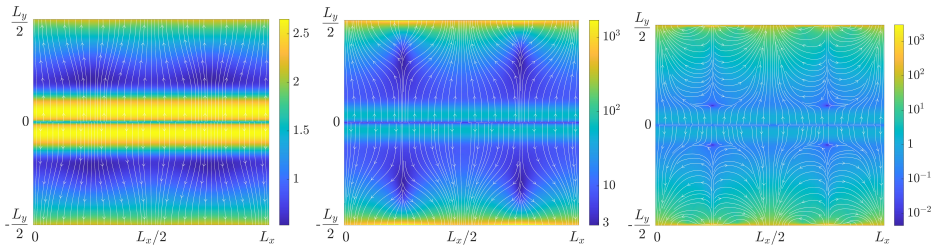

(a) $\|\mathcal{H}_e\|_\infty = 10$. (b) $\|\mathcal{H}_e\|_\infty = 10^2$. (c) $\|\mathcal{H}_e\|_\infty = 10^3$ (log. scale).

Figure 8: Electric field magnitude ($\mathrm{V} \cdot \mathrm{m}^{-1}$) in a color scale and associated field lines for different magnetisation intensities.

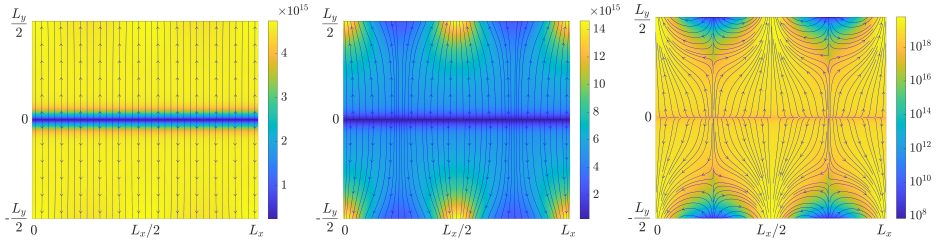

(a) $\|\mathcal{H}_e\|_\infty = 10$. (b) $\|\mathcal{H}_e\|_\infty = 10^2$. (c) $\|\mathcal{H}_e\|_\infty = 10^3$ (log. scale).

Figure 9: Ionic flux density $\Gamma_i = nu_i$ ($\mathrm{m}^{-2} \cdot \mathrm{s}^{-1}$) for different magnetisation intensities.

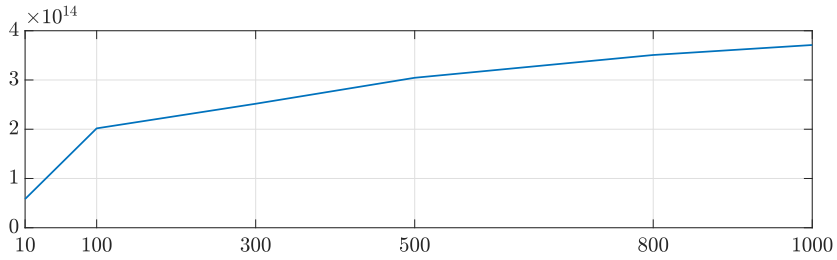

Figure 10: Number of confined particles in the inter-electrode chamber as a function of the Hall parameter $\|\mathcal{H}_e\|_\infty$.

confirms the confinement of the plasma thanks to its magnetization. This confinement is also observed on the density and flux profiles along the electrodes (Fig. 11). The particles are escaping the inter-electrode chamber along channels located in the regions of the magnetic field cusps. The width of these channels is narrowed with the increase of the magnetic field intensity. This is qualitatively in line with the observations reported in [25].

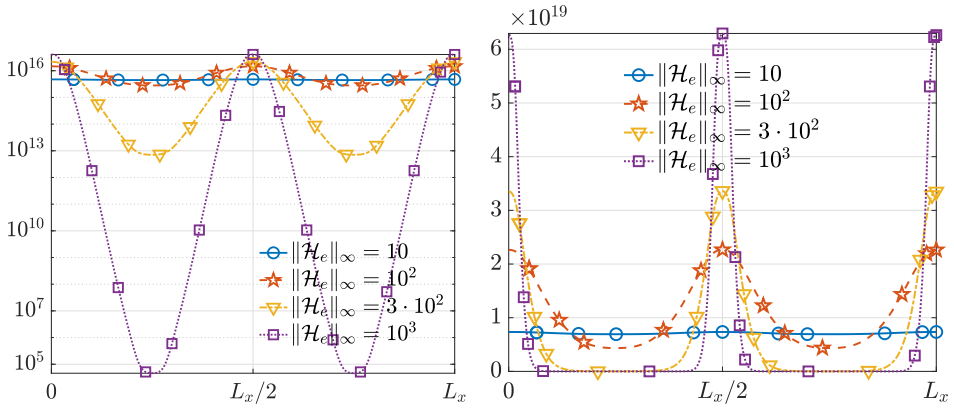

(a) Density profile as a function of x (m^{-3}).

(b) $\Gamma_i \cdot \boldsymbol{n}$ as a function of x ($\mathrm{m}^{-2} \cdot \mathrm{s}^{-1}$).

Figure 11: Profile of the plasma density and ionic flux density along the electrodes for different intensities of magnetic field.

4.2.2 Inflow versus Augmented Micro-Macro formulations

In this section, the loss of symmetry of solutions carried out thanks to the classical Micro-Macro method is outlined and compared to the outputs of the augmented version introduced in this work. These two methods differ by the subset of nodes used to imposing a condition on the auxiliary variable in order to restore uniqueness of the problem. Classically this condition is set on the subset of the boundary onto which the magnetic field inflows the domain ($b \cdot \boldsymbol{n} > 0$). For the magnetic field geometry considered here, this amounts to prescribing this condition on nodes of the boundary materialized by the red dotted lines on the plots of Fig. (12a). The discrete problem is therefore non symmetric with respect to the localization of the nodes where q is set to 0. This is experienced to produce numerical approximations inconsistent with the problem symmetries. The symmetry breakdown accumulates over the iterations, providing the plots of Fig. 12c representing the profiles of the steady state electric potential on both electrodes. These curves are non symmetric, similarly to the distribution on each boundaries of the nodes selected to prescribe the inflow condition $q = 0$.

The augmented Micro-Macro formulation operates nodes distributed on different locations as plotted on Fig. 12b. The subset $\partial\Omega_0$ intersects every magnetic field lines, however with a symmetric distribution in the computational domain. The augmented formulation offers the possibility to restore the symmetry of the solution: the curves associated to both electrodes are perfectly matching as shown on Fig. 12d, the difference of the two profiles being comparable to the computer arithmetic precision.

All the plots presented in Sec. 4.2.1 are related to computations carried out thanks to the augmented Micro-Macro method.

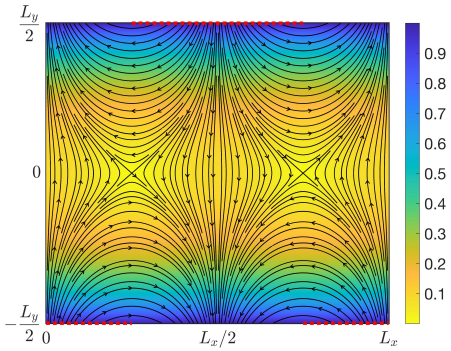

(a) Subset $\partial\Omega_0$ for the inflow method.

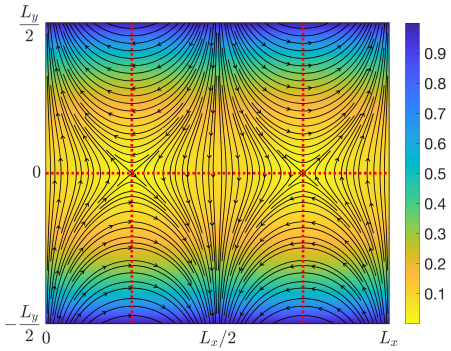

(b) Subset $\partial\Omega_0$ for the augmented method.

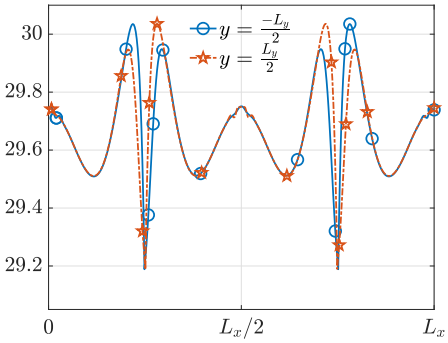

(c) Electric potential profiles carried out with the inflow method.

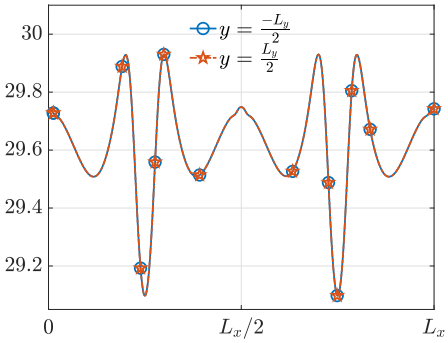

(d) Electric potential profiles carried out with the augmented method.

Figure 12: Definition of the subset $\partial\Omega_0$ (red dotted lines) used to restore the well-posedness of the problem for the inflow (a) and the augmented (b) Micro-Macro (MM) methods; Profiles of the steady state electric potential along the electrodes: blue plain line with circles for $\phi(x, {}^{-L_y}/_2)$ and red dashed dotted line with pentagrams for $\phi(x, {}^{L_y}/_2)$, $\|\mathcal{H}_e\|_\infty = 3 \cdot 10^2$.

4.2.3 On the robustness of the numerical model

The large depletion of the density inside the quasi-vacuum basins calls into question the relevance of the quasi-neutrality assumption embedded in the model. This question is investigated thanks to two diagnostics. The first one is the scaled Debye length obtained for $\mathcal{H}_e = 10^3$ as displayed on Fig. 13a. The level-sets $\lambda = 1$ plotted on this figure dissociate the validity domain of the quasi-neutral assumption ($\lambda \lesssim 1$) from regions where the typical scale (the mesh size) is comparable or smaller to the local (physical) Debye length.

The second diagnostic is the ratio of the magnitude of the two contributions carrying the electric field in the non quasi-neutral model presented in Sec. 2.3.2. Two distinct inputs are indeed involved in the equation satisfied by the electric

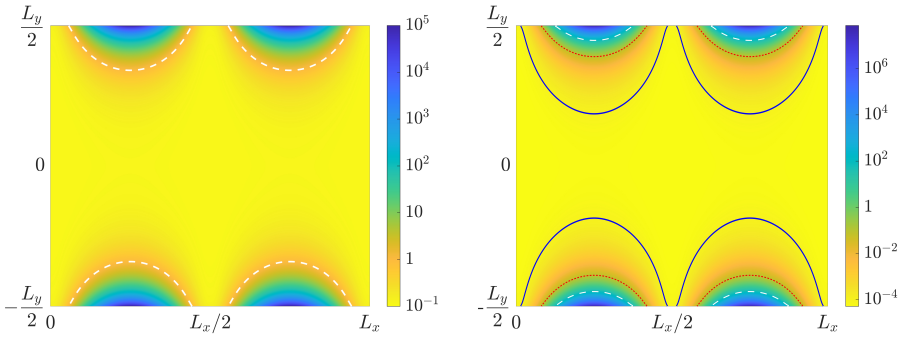

(a) Dimensionless Debye length $\bar{\lambda}$.

(b) Quasi-neutrality parameter γ_{QN}.

Figure 13: Breakdown of the quasi-neutrality assumption: (a) Dimensionless Debye length in a logarithmic color scale, the level-set $\bar{\lambda} = 1$ is plotted in a dashed white line; (b) Squared dimensionless Debye length related to the product of the squared electronic Mach number and the number of collisions per typical time $\gamma_{\mathrm{QN}} = \lambda^2 M_e^2 \kappa_e$ in a color logarithmic scale. The level-sets $\gamma_{\mathrm{QN}} = 1$, 10^3 and 10^6 are plotted in a dashed white, dashed-dotted red and plain blue lines.

potential as defined by Eqs. (19). The first one originates from the classical isotropic Poisson operator. It is carried by the scaled Debye length in the dimensionless framework introduced herein. The anisotropy is introduced into this equation by means of the electronic mobility tensor issued from the divergence of the electronic current. This second contribution is proportional to $1/(M_e^2\kappa_e)$. The balance between these two contributions is evaluated by $\gamma_{\mathrm{QN}} = \lambda^2 M_e^2 \kappa_e$. The value of this parameter is plotted on Fig. 13b. It is evaluated thanks to the local density, the time step and mesh size being used as typical values for the time and length scales. The regions delimited by the electrodes and the level-sets $\gamma_{\mathrm{QN}} = 1$ materialize locations where the non quasi-neutral contribution is dominant in Eq. (19a). In between this level-set and the one associated to $\gamma_{\mathrm{QN}} = \varepsilon^{-1} = 10^6$, the non quasi-neutral (isotropic) contributions exceed the magnitude of the diagonal coefficient of the anisotropic tensor in Eq. (19a). In other words, non quasi-neutral corrections should significantly decrease the anisotropy of this equation in regions delimited by the electrodes and level-set $\gamma_{\mathrm{QN}} = \varepsilon^{-1} = 10^6$, entailing possible changes of the electric field inside the quasi-vacuum basins. Contrariwise, in the channels where the particles are flowing outside the domain, the quasi-neutral assumption is valid, a feature that should be further consolidated for simulations carried out with larger plasma densities.

These observations outline that the computations performed herein are quite demanding with respect to the anisotropy embedded into the system matrix providing the electric potential. Furthermore, this matrix exhibits a condition number deteriorating with the vanishing of the density. This is related to the

fact that the continuity equation used to carry out the electric potential is close to singularity because of the small plasma density values. The robustness of the model shall be pointed out and these difficulties are related to the (quasi-neutral) model supporting these investigations. These difficulties shall be overcome by supplementing the model with non quasi-neutral corrections which amounts to make a step backward in the model hierarchy represented on Fig 1 and implement the transition from the quasi-neutral drift diffusion model (as defined in Sec. 2.3.3) to the Drift-Diffusion-Poisson system (Sec. 2.3.2) in which the quasi-neutral assumption is revoked.

5 Conclusions

In this paper a hierarchy of fluid models is proposed for the simulation of low temperature plasmas confined by intense magnetic fields. The derivation of these models unravels the different assumptions embedded in the equations widely implemented for the simulation in the framework of electric propulsion. The issue related to the approximation of anisotropic problems present in quasi-neutral modelling of magnetically confined plasmas is addressed by means of asymptotic preserving methods. These methods provide numerical approximation with an accuracy unrelated to the anisotropy strength using coordinates and meshes misaligned with the magnetic direction. A new formulation of the so-called Micro-Macro method is proposed in order to restore the symmetry of the problem that is lost in the existing (inflow Micro-Macro) method. The validation of the augmented method is conducted thanks to an analytic framework. The method is proved to be accurate regardless of the anisotropy strength. This method is implemented for the quasi-neutral simulation of a plasma confined by a cusp-shaped magnetic field, with parameters representative of the electric propulsion. Though the model remains quite coarse, the confinement of the plasma is accounted for by the numerical method proposed within this document. Nonetheless, a refined description of the ionization process is mandatory. It is indeed determinant for the plasma dynamics, and strongly related to the electronic temperature. The model shall therefore be upgraded with an electronic energy equation, which remains a real challenge for numerical methods. The electronic dynamics is indeed stiff and strongly anisotropic. This perspective outlines the tremendous importance of developing numerical methods precise regardless of the anisotropy strength.

Acknowledgements

This work has been supported by the RTRA STAE fondation in the frame of the INNPULSE project (InNovative CoNcepts for Plasma PropULsion in Space) and by a public grant from the “Laboratoire d’Excellence Centre International de Mathématiques et d’Informatique” (LabEx CIMI) overseen by the French National Research Agency (ANR) as part of the “Investissements d’Avenir”

program (reference ANR-11-LABX-0040) in the frame of the PROMETEUS project (PRospect of nOvel nuMerical modEls for elecTric propulsion and low tEmperatUre plaSmas).
F.D. and J.N. acknowledge support from the FrFCM (Fédération de recherche pour la Fusion par Confinement Magnétique) in the frame of the NEMESIA project (Numerical mEthods for Macroscopic models of magnEtized plaSmas and related anIsotropic equAtions).

References

[1] A. Alvarez-Laguna. Plasma-sheath transition in multi-fluid models with inertial terms under low pressure conditions: comparison with the classical and kinetic theory. *Plasma Sources Sci. Technol.*, page 16, 2020.

[2] A. Alvarez Laguna, T. Pichard, T. Magin, P. Chabert, A. Bourdon, and M. Massot. An asymptotic preserving well-balanced scheme for the isothermal fluid equations in low-temperature plasmas at low-pressure. *Journal of Computational Physics*, 419:109634, Oct. 2020.

[3] J. Bareilles, G. J. M. Hagelaar, L. Garrigues, C. Boniface, J. P. Boeuf, and N. Gascon. Critical assessment of a two-dimensional hybrid Hall thruster model: Comparisons with experiments. *Physics of Plasmas*, 11(6):3035–3046, June 2004.

[4] C. Besse, P. Degond, F. Deluzet, J. Claudel, G. Gallice, and C. Tessieras. A model hierarchy for ionospheric plasma modeling. *Mathematical Models and Methods in Applied Sciences*, 14(03):393–415, Mar. 2004.

[5] S. Boccelli, T. Charoy, A. Alvarez Laguna, P. Chabert, A. Bourdon, and T. E. Magin. Collisionless ion modeling in Hall thrusters: Analytical axial velocity distribution function and heat flux closures. *Physics of Plasmas*, 27(7):073506, July 2020.

[6] J.-P. Boeuf. Tutorial: Physics and modeling of Hall thrusters. *Journal of Applied Physics*, 121(1):011101, Jan. 2017.

[7] J. P. Boeuf and L. Garrigues. E × B electron drift instability in Hall thrusters: Particle-in-cell simulations vs. theory. *Physics of Plasmas*, 25(6):061204, June 2018.

[8] A. S. Chamarthi, K. Komurasaki, and R. Kawashima. High-order upwind and non-oscillatory approach for steady state diffusion, advection–diffusion and application to magnetized electrons. *Journal of Computational Physics*, 374:1120–1151, Dec. 2018.

[9] T. Charoy, T. Lafleur, A. Tavant, P. Chabert, and A. Bourdon. A comparison between kinetic theory and particle-in-cell simulations of anomalous electron transport in E × B plasma discharges. *Physics of Plasmas*, 27(6):063510, June 2020.

[10] R. Chodura. Plasma Flow in the Sheath and the Presheath of a Scrape-Off Layer. In D. E. Post and R. Behrisch, editors, *Physics of Plasma-Wall Interactions in Controlled Fusion*, pages 99–134. Springer US, Jan. 1986.

[11] A. Crestetto, F. Deluzet, and D. Doyen. Bridging kinetic plasma descriptions and single-fluid models. *Journal of Plasma Physics*, 86(5), Oct. 2020.

[12] P. Crispel, P. Degond, and M.-H. Vignal. Quasi-neutral fluid models for current-carrying plasmas. *Journal of Computational Physics*, 205(2):408–438, May 2005.

[13] P. Crispel, P. Degond, and M.-H. Vignal. An asymptotic preserving scheme for the two-fluid Euler–Poisson model in the quasineutral limit. *Journal of Computational Physics*, 223(1):208–234, Apr. 2007.

[14] V. Croes. 2D particle-in-cell simulations of the electron drift instability and associated anomalous electron transport in Hall-effect thrusters. *Plasma Sources Sci. Technol.*, page 15, 2017.

[15] P. Degond and F. Deluzet. Asymptotic-Preserving methods and multiscale models for plasma physics. *Journal of Computational Physics*, 336:429–457, May 2017.

[16] P. Degond, F. Deluzet, A. Lozinski, J. Narski, and C. Negulescu. Duality-based Asymptotic-Preserving method for highly anisotropic diffusion equations. *Commun. Math. Sci.*, 10(1):1–31, 2012.

[17] P. Degond, F. Deluzet, and C. Negulescu. An asymptotic preserving scheme for strongly anisotropic elliptic problems. *Multiscale Modeling & Simulation. A SIAM Interdisciplinary Journal*, 8(2):645–666, Oct. 2009.

[18] P. Degond, F. Deluzet, and D. Savelief. Numerical approximation of the Euler–Maxwell model in the quasineutral limit. *Journal of Computational Physics*, 231(4):1917–1946, Feb. 2012.

[19] P. Degond, A. Lozinski, J. Narski, and C. Negulescu. An asymptotic-preserving method for highly anisotropic elliptic equations based on a Micro-Macro decomposition. *Journal of Computational Physics*, 231(7):2724–2740, 2012.

[20] F. Deluzet and J. Narski. A Two Field Iterated Asymptotic-Preserving Method for Highly Anisotropic Elliptic Equations. *Multiscale Modeling & Simulation*, pages 434–459, Jan. 2019.

[21] S. Günter, Q. Yu, J. Krüger, and K. Lackner. Modelling of heat transport in magnetised plasmas using non-aligned coordinates. *J. Comput. Phys.*, 209(1):354–370, Oct. 2005.

[22] G. J. M. Hagelaar. Modelling electron transport in magnetized low-temperature discharge plasmas. *Plasma Sources Science and Technology*, 16(1):S57, 2007.

[23] G. J. M. Hagelaar, J. Bareilles, and L. Garrigues. Two-dimensional model of a stationary plasma thruster. *J. Appl. Phys.*, 91(9):8, 2002.

[24] J. D. Huba. NRL PLASMA FORMULARY. Technical report, Naval Research Lab., Washington, DC 20375, 2011.

[25] Y. Jiang, G. Fubiani, L. Garrigues, and J. P. Boeuf. Magnetic cusp confinement in low-β plasmas revisited. *Physics of Plasmas*, page 14, 2020.

[26] I. D. Kaganovich, A. Smolyakov, Y. Raitses, E. Ahedo, I. G. Mikellides, B. Jorns, F. Taccogna, R. Gueroult, S. Tsikata, A. Bourdon, M. Keidar, A. T. Powis, M. Merino, M. Cappelli, K. Hara, N. J. Fisch, P. Chabert, I. Schweigert, T. Lafleur, K. Matyash, A. V. Khrabrov, R. W. Boswell, and A. Fruchtman. Physics of E $\times$ B discharges relevant to plasma propulsion and similar technologies. *Physics of Plasmas*, page 46, 2020.

[27] R. Kawashima, K. Komurasaki, and T. Schönherr. A hyperbolic-equation system approach for magnetized electron fluids in quasi-neutral plasmas. *Journal of Computational Physics*, 284:59–69, Mar. 2015.

[28] R. Kawashima, K. Komurasaki, and T. Schönherr. A flux-splitting method for hyperbolic-equation system of magnetized electron fluids in quasi-neutral plasmas. *Journal of Computational Physics*, 310:202–212, Apr. 2016.

[29] T. Lafleur, R. Martorelli, P. Chabert, and A. Bourdon. Anomalous electron transport in Hall-effect thrusters: Comparison between quasi-linear kinetic theory and particle-in-cell simulations. *Phys. Plasmas*, page 13, 2018.

[30] I. Levchenko, S. Xu, S. Mazouffre, D. Lev, D. Pedrini, D. Goebel, L. Garrigues, F. Taccogna, and K. Bazaka. Perspectives, frontiers, and new horizons for plasma-based space electric propulsion. *Physics of Plasmas*, 27(2):020601, Feb. 2020.

[31] M. A. Lieberman and A. J. Lichtenberg. *Principles of Plasma Discharges and Materials Processing*. Wiley-Blackwell, Hoboken, N.J, 2nd edition edition, May 2005.

[32] A. Lopez Ortega, I. G. Mikellides, M. J. Sekerak, and B. A. Jorns. Plasma simulations in 2-D (r-z) geometry for the assessment of pole erosion in a magnetically shielded Hall thruster. *Journal of Applied Physics*, 125(3):033302, Jan. 2019.

[33] I. G. Mikellides and I. Katz. Numerical simulations of Hall-effect plasma accelerators on a magnetic-field-aligned mesh. *Physical Review E*, 86(4):046703, Oct. 2012.

[34] A. I. Morozov and V. V. Savelyev. Fundamentals of Stationary Plasma Thruster Theory. In *Reviews of Plasma Physics*, pages 203–391. Springer US, Boston, MA, 2000.

[35] S. Sadouni. *Fluid modeling of transport and instabilities in magnetized low-temperature plasma sources*. Theses, Université Paul Sabatier - Toulouse III, Feb. 2020.

[36] R. Sahu, A. R. Mansour, and K. Hara. Full fluid moment model for low temperature magnetized plasmas. *Physics of Plasmas*, 27(11):113505, Nov. 2020.

[37] A. Sengupta. Magnetic confinement in a ring-cusp ion thruster discharge plasma. *J. Appl. Phys.*, 105(9):11, Feb. 2009.

[38] F. Taccogna and L. Garrigues. Latest progress in Hall thrusters plasma modelling. *Reviews of Modern Plasma Physics*, 3(1):12, Dec. 2019.

[39] C. Yang, J. Claustre, and F. Deluzet. Iterative Solvers for Elliptic Problems with Arbitrary Anisotropy Strengths. *Multiscale Modeling & Simulation*, 16(4):1795–1823, Jan. 2018.

[40] C. Yang, F. Deluzet, and J. Narski. On the numerical resolution of anisotropic equations with high order differential operators arising in plasma physics. *Journal of Computational Physics*, 386:502–523, June 2019.

[41] C. Yang, F. Deluzet, and J. Narski. Preserving the accuracy of numerical methods discretizing anisotropic elliptic problems. *arXiv:1911.11482 [cs, math]*, Nov. 2019. arXiv: 1911.11482.

A Time and space discretizations

We introduce the Cartesian, homogeneous grid of the time-space $(0,\infty)\times\Omega$

$$((k-1)\Delta t,(i-1)\Delta x,(i-1)\Delta y)_{k\in\mathbb{N}^*,i\in[\![1,N_x]\!],j\in[\![1,N_y]\!]}$$

where Δt is the time step, Δx and Δy are the space steps, N_x and N_y are positive integers. We set

$$\psi^k_{i,j}=\psi(k\Delta t,i\Delta x,j\Delta y),q^k_{i,j}=q(k\Delta t,i\Delta x,j\Delta y),\quad n^k_{i,j}=n(k\Delta t,i\Delta x,j\Delta y),$$
$$v^k_{x,i,j}=v_x(k\Delta t,i\Delta x,j\Delta y),\quad v^k_{y,i,j}=v_y(k\Delta t,i\Delta x,j\Delta y).$$

The spatial discretization of the electronic system (41) is carried out with the "asymmetric" finite difference scheme proposed in [21, 41]. For a given flux

$$F=\begin{bmatrix}a_{xx} & a_{xy}\\ a_{xy} & a_{yy}\end{bmatrix}\nabla\psi,$$

the finite approximation of $\nabla\cdot F$ is

$$-\frac{1}{\Delta x}\left(F_{x,i+\frac{1}{2},j}-F_{x,i-\frac{1}{2},j}\right)-\frac{1}{\Delta y}\left(F_{y,i,j+\frac{1}{2}}-F_{y,i,j-\frac{1}{2}}\right),$$

where the discrete flux $\begin{bmatrix} F_{x,i+\frac{1}{2},j} & F_{y,i,j+\frac{1}{2}} \end{bmatrix}^T$ associated to F are defined at the cell interfaces thanks to

$$\begin{cases} F_{x,i+\frac{1}{2},j} = \dfrac{a_{xx,i+\frac{1}{2},j}}{\Delta x}\left(\psi^k_{i+1,j} - \psi^k_{i,j}\right) \\ \qquad\qquad + \dfrac{a_{xy,i+\frac{1}{2},j}}{4\Delta y}\left((\psi^k_{i+1,j+1} + \psi^k_{i,j+1}) - (\psi^k_{i+1,j-1} + \psi^k_{i,j-1})\right), \\ F_{y,i,j+\frac{1}{2}} = \dfrac{a_{xy,i,j+\frac{1}{2}}}{4\Delta x}\left((\psi^k_{i+1,j+1} + \psi^k_{i+1,j}) - (\psi^k_{i-1,j} + \psi^k_{i-1,j})\right) \\ \qquad\qquad\qquad\qquad + \dfrac{a_{yy,i,j+\frac{1}{2}}}{\Delta y}\left(\psi^k_{i,j+1} - \psi^k_{i,j}\right). \end{cases} \tag{44}$$

Thanks to that scheme, the approximation of system (41) writes

$$\begin{cases} -\dfrac{1}{\Delta x}\left(F^k_{x,i+\frac{1}{2},j} - F^k_{x,i-\frac{1}{2},j}\right) \\ \qquad\qquad - \dfrac{1}{\Delta y}\left(F^k_{y,i,j+\frac{1}{2}} - F^k_{y,i,j-\frac{1}{2}}\right) + \mathscr{L}^k_{i_0,j_0} = S^k_{i,j}, \\ -\dfrac{1}{\Delta x}\left(G^k_{x,i+\frac{1}{2},j} - G^k_{x,i-\frac{1}{2},j}\right) - \dfrac{1}{\Delta y}\left(G^k_{y,i,j+\frac{1}{2}} - G^k_{y,i,j-\frac{1}{2}}\right) = 0, \\ q_{i_0,j_0} = 0\,, \\ F^k_{x,\frac{1}{2},j} = 0, \quad F^k_{x,N_x-\frac{1}{2},j} = 0, \quad q_{1,j} = 0, \quad q_{N_x,j} = 0, \\ F_{y,i,\frac{1}{2}} = -\left[\Gamma_\beta\left(-\psi + k_B T_e \ln\left(\dfrac{n}{n_0}\right)\right)\right]^k_{i,\frac{1}{2}}, \quad G^k_{y,i,\frac{1}{2}} = 0, \\ F^k_{y,i,N_y-\frac{1}{2}} = \left[\Gamma_\beta\left(-\psi + k_B T_e \ln\left(\dfrac{n}{n_0}\right)\right)\right]^k_{i,N_y-\frac{1}{2}}, \quad G^k_{y,i,N_y-\frac{1}{2}} = 0, \end{cases} \tag{45}$$

where $(i_0, j_0) \in \mathcal{I}_0$, $\mathcal{I}_0$ being a subset of $[\![1, N_x]\!] \times [\![1, N_y]\!]$ discretizing $\partial\Omega_0$ and $\begin{bmatrix} F^k_{x,i+\frac{1}{2},j} & F^k_{y,i,j+\frac{1}{2}} \end{bmatrix}^T$ and $\begin{bmatrix} G^k_{x,i+\frac{1}{2},j} & G^k_{y,i,j+\frac{1}{2}} \end{bmatrix}^T$ are discrete fluxes associated to

$$F^k = \mu n^k \varepsilon \nabla_\parallel q + \mu n^k \varepsilon \nabla_\perp \psi \quad \text{ and } \quad G^k = \mu n^k \varepsilon \nabla_\parallel q - \mu n^k \nabla_\parallel \psi\,,$$

defined accordingly to Eqs. (44).

System (1) describing the evolution of the ions is discretized by means of a Rusanov scheme

$$\begin{cases} n^{k+1}_{i,j} = n^k_{i,j} - \dfrac{\Delta t}{\Delta x}\left(H^k_{x,i+\frac{1}{2},j} - H^k_{x,i-\frac{1}{2},j}\right) - \\ \qquad\qquad\qquad\qquad \dfrac{1}{\Delta y}\left(H^k_{y,i,j+\frac{1}{2}} - H^k_{y,i,j-\frac{1}{2}}\right) + \Delta t S^k_{i,j} \\ n^{k+1}_{1,j} = n^{k+1}_{2,j}, \quad n^{k+1}_{N_x,j} = n^{k+1}_{N_x-1,j}, \\ n^{k+1}_{i,1} = \dfrac{n^k_{i,2} v^k_{y,i,2}}{v_B}, \quad n^{k+1}_{i,N_y} = \dfrac{n^k_{i,N_y-1} v^k_{y,i,N_y-1}}{v_B}, \end{cases} \tag{46}$$

$$
\begin{cases}
n_{i,j}^{k+1} v_{x,i,j}^{k+1} = n_{i,j}^k v_{x,i,j}^k \dfrac{\Delta t}{\Delta x}\left(M_{x,i+\frac{1}{2},j}^k - M_{x,i-\frac{1}{2},j}^k\right) - \\
\qquad\qquad - \dfrac{\Delta t}{\Delta y}\left(M_{y,i,j+\frac{1}{2}}^k - M_{y,i,j-\frac{1}{2}}^k\right) + \dfrac{e\Delta t}{m_i} n_{i,j}^k E_{x,i,j}^k, \\
n_{i,j}^{k+1} v_{y,i,j}^{k+1} = n_{i,j}^k v_{y,i,j}^k - \dfrac{\Delta t}{\Delta x}\left(L_{x,i+\frac{1}{2},j}^k - L_{x,i-\frac{1}{2},j}^k\right) \\
\qquad\qquad - \dfrac{\Delta t}{\Delta y}\left(L_{y,i,j+\frac{1}{2}}^k - L_{y,i,j-\frac{1}{2}}^k\right) + \dfrac{e\Delta t}{m_i} n_{i,j}^k E_{y,i,j}^k, \\
v_{x,1,j}^{k+1} = 0, \quad v_{x,N_x,j}^{k+1} = 0, \quad v_{y,i,1}^{k+1} = -1, \quad v_{y,i,N_y}^{k+1} = 1,
\end{cases}
\tag{47}
$$

where

$$
\begin{aligned}
H_{x,i+\frac{1}{2},j}^k &= n_{i+1,j}^k v_{x,i+1,j}^k + n_{i,j}^k v_{x,i,j}^k + \Lambda_{i+\frac{1}{2},j}^k (n_{i+1,j}^k - n_{i,j}^k), \\
H_{y,i,j+\frac{1}{2}}^k &= n_{i,j+1}^k v_{y,i,j+1}^k + n_{i,j}^k v_{y,i,j}^k + \Lambda_{i,j+\frac{1}{2}}^k (n_{i,j+1}^k - n_{i,j}^k), \\
M_{x,i+\frac{1}{2},j}^k &= n_{i+1,j}^k v_{x,i+1,j}^k v_{x,i+1,j}^k + n_{i,j}^k v_{x,i,j}^k v_{x,i,j}^k + \\
&\qquad \Lambda_{i+\frac{1}{2},j}^k (n_{i+1,j}^k v_{x,i+1,j}^k - n_{i,j}^k v_{x,i,j}^k), \\
L_{x,i+\frac{1}{2},j}^k &= n_{i+1,j}^k v_{y,i+1,j}^k v_{x,i+1,j}^k + n_{i,j}^k v_{y,i,j}^k v_{x,i,j}^k + \\
&\qquad \Lambda_{i+\frac{1}{2},j}^k (n_{i+1,j}^k v_{y,i+1,j}^k - n_{i,j}^k v_{y,i,j}^k),
\end{aligned}
$$

the fluxes $M_{y,i,j+\frac{1}{2}}^k$ and $L_{y,i,j+\frac{1}{2}}^k$ being defined similarly, and

$$
\Lambda_{i+\frac{1}{2},j}^k = \frac{\Delta t}{2\Delta x}(2 + |v_{x,i+1,j}^k| + |v_{x,i,j}^k|), \quad \Lambda_{i,j+\frac{1}{2}}^k = \frac{\Delta t}{2\Delta y}(2 + |v_{y,i,j+1}^k| + |v_{y,i,j}^k|).
$$

The numerical viscosity of the scheme is lower bounded by a positive value, arbitrarily set to 1, to ensure the stability of the scheme in regions where the plasma may be at rest. The value of this threshold has not been experienced to be significant in the simulation outputs.

The approximation of the electric field $E = -\nabla\phi$ is defined as

$$
E_{x,i+1/2,j}^k = -\frac{\phi_{i+1,j} - \phi_{i,j}}{\Delta x} \quad \text{and} \quad E_{y,i,j+1/2}^k = -\frac{\phi_{i,j+1} - \phi_{i,j}}{\Delta y}.
$$